Rep. Prog. Phys. **75** (2012) 096501 (23pp) doi:10.1088/0034-4885/75/9/096501

Topological materials

Binghai Yan and Shou-Cheng Zhang

Department of Physics, Stanford University, Stanford, CA 94305, USA

E-mail: sczhang@stanford.edu

Received 3 November 2011, in final form 20 April 2012
Published 20 August 2012
Online at stacks.iop.org/RoPP/75/096501

Abstract

Recently, topological insulator materials have been theoretically predicted and experimentally observed in both 2D and 3D systems. We first review the basic models and physical properties of topological insulators, using HgTe and Bi_2Se_3 as prime examples. We then give a comprehensive survey of topological insulators which have been predicted so far, and discuss the current experimental status.

(Some figures may appear in colour only in the online journal)

This article was invited by P Coleman.

Contents

1. Introduction

Topological insulators (TIs) are recently discovered new states of quantum matter [1–4]. They have a full energy gap in the bulk and gapless edge or surface states, which are topologically protected by time reversal symmetry (TRS). The edge states of two-dimensional (2D) TIs are protected from backscattering, and can carry currents along the edge channel without dissipation. Three-dimensional (3D) TIs are fundamentally characterized by a topological magneto-electric effect with a quantized response coefficient.

TI materials have been theoretically predicted and experimentally observed in a variety of materials. Since the development of the theoretical concepts [5, 6] and the first discovery of TIs in the HgTe system [7, 8], the number of known TIs has increased dramatically. In this review, we give an up-to-date survey of these materials, discuss theoretical predictions and experimental observations.

2. Two-dimensional topological insulators: HgTe quantum wells

The 2D TI, also known as the quantum spin Hall (QSH) state, was first discovered in HgTe quantum wells (QWs). In 2006 Bernevig, Hughes and Zhang [7] (BHZ) proposed a general mechanism for finding TIs and in particular predicted that HgTe/CdTe QWs—nanoscale HgTe thin films sandwiched between two conventional insulating layers of CdTe—are TIs with a quantum phase transition as a function of thickness d_{QW}. The QW is predicted to be a 2D TI with a single pair of helical edge states for $d_{QW} > d_c$ and a conventional insulator for $d_{QW} < d_c$, where d_c is the critical thickness. The general mechanism is band inversion, in which the usual band ordering of the conduction band and valence band is 'inverted' by spin–orbit coupling (SOC) [7]. This mechanism serves as a template for most TIs discovered later. Soon after the theoretical prediction, the 2D TI or QSH state was observed experimentally in HgTe QWs [8].

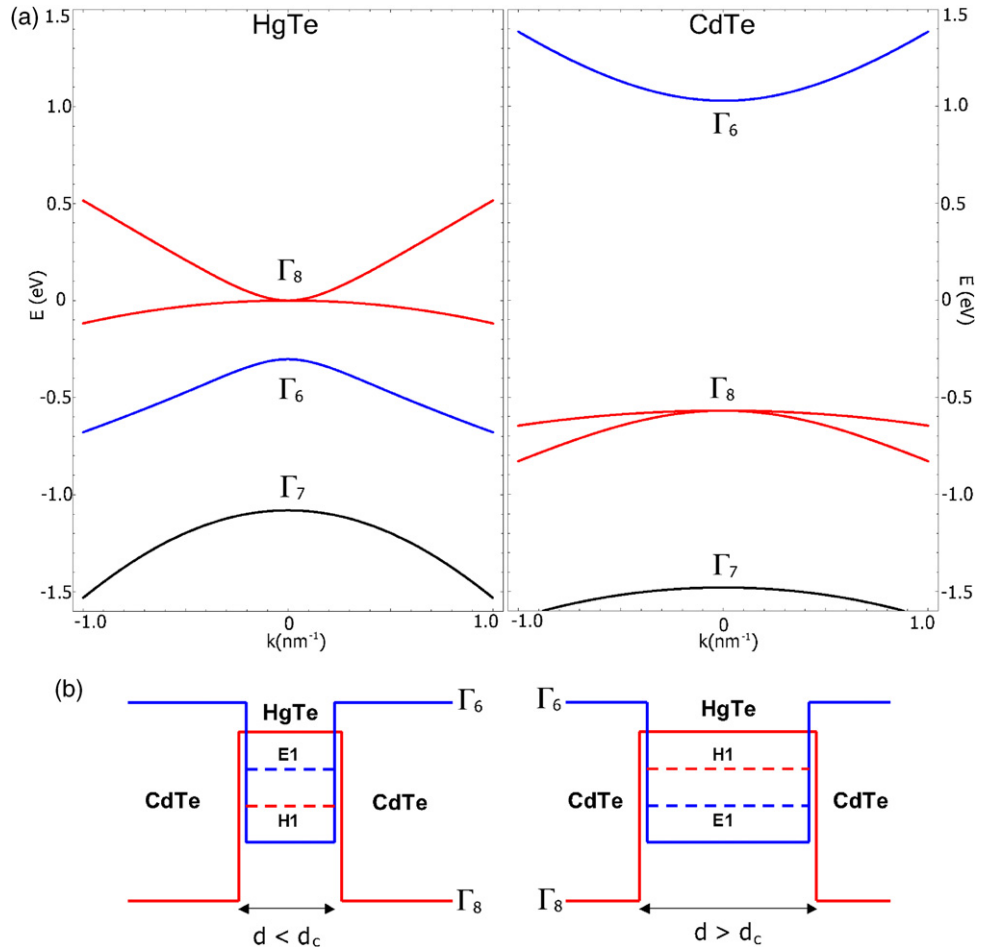

Figure 1. (*a*) Bulk band (BB) structure of HgTe and CdTe; (*b*) schematic picture of QW geometry and lowest subbands for two different thicknesses. Adapted with permission from [7]. Copyright 2006 American Association for the Advancement of Science.

2.1. Model Hamiltonian for HgTe

Both HgTe and CdTe have zinc-blende lattice structure like diamond, in which two interpenetrating face-centered-cubic (fcc) lattices are shifted along the body diagonal. Their low-energy bands near the Fermi level are close to the Γ point in the Brillouin zone, as shown in figure 1. They are an s-orbital band (labeled Γ_6 by symmetry), a p-orbital band split by SOC into a $J = 3/2$ band (labeled Γ_8) and a $J = 1/2$ band (labeled Γ_7). Here the Γ_8 band can be further classified into heavy-hole ($m_J = \pm 3/2$) and light-hole bands ($m_J = \pm 1/2$) by the effective mass. Like the common semiconductor GaAs, CdTe has a band ordering with Γ_6 as the conduction band minimum (CBM) and Γ_8 as the valence band maximum (VBM). The CBM and VBM are separated by a large energy gap of ∼1.6 eV. Compared with Cd, Hg is a heavier element and has stronger relativistic effects. As a result of both the Darwin term and the SOC, HgTe exhibits an 'inverted' band ordering: the Γ_8 band is shifted above the Γ_6 band. The Γ_6 band lies about 300 meV below the Γ_8 band, but far above the split-off Γ_7 band. The light-hole and heavy-hole bands become CBM and VBM, respectively. Due to cubic symmetry these two bands are degenerate at the Γ point. Therefore, HgTe is a zero-gap semiconductor with an inverted band ordering.

HgTe can open an energy gap when the cubic symmetry is broken by strain or by lower dimensionality. The conventional semiconductor CdTe serves as an ideal barrier layer for QWs due to its larger energy gap and well-matched crystal structure. When CdTe/HgTe/CdTe QWs are fabricated, the inverted band structure of HgTe can be used to tune the electronic properties by varying the QW thickness $d_{\rm QW}$. In QWs, Γ_6 and Γ_8 bands combine to form spin-up and spin-down (±) states of three QW subbands: E_n, H_n and L_n, where the subscript $n = 1, 2, 3, \ldots$ describes the QW states with increasing number of nodes in the QW growth z direction. The L_n subband is separated from the other two and can be neglected. The H_n subbands are derived from the heavy-hole Γ_8 band and E_n from the Γ_6 electron band and the Γ_8 light-hole band. Very thin QWs should behave similarly to CdTe and have normal band ordering, i.e. the QW subbands having primarily Γ_6 symmetry (E_n) are conduction bands and subbands with Γ_8 symmetry (H_n) are valence bands, E_1 and H_1 are CBM and VBM, respectively. On the other hand, very wide QWs should behave more like HgTe with inverted bands. As $d_{\rm QW}$ increases from the very thin case, E_n bands are pulled down and H_n bands are pushed up. E_1 and H_1 are expected to cross at a critical thickness and become inverted: E_1 from Γ_6 becomes the valence band and H_1 from Γ_8 becomes the conduction band. The energy levels versus $d_{\rm QW}$ dependence is shown in figure 2. The inversion between E_1 and H_1 bands happens at a critical thickness $d_{\rm QW} = d_{\rm c} \sim 6.3$ nm. In the following, we introduce the BHZ

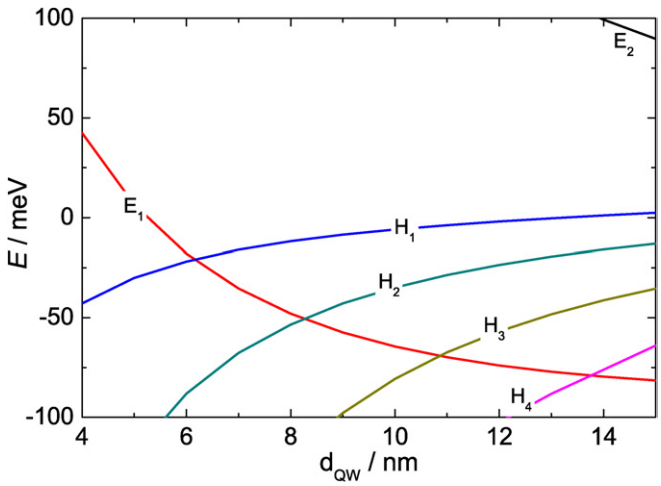

Figure 2. Energy levels of the QW as a function of QW width. Adapted with permission from [9]. Copyright 2008 The Physical Society of Japan.

model and illustrate the 2D TI with protected edge states for QWs with $d_{\rm QW} > d_{\rm c}$.

HgTe has a zinc-blende structure which lacks inversion symmetry. However, inversion symmetry breaking has only a small effect on the physics of the topological insulator. For simplicity of discussion, we first assume inversion symmetry for HgTe. Since TRS is present, the VBM E_1 and the CBM H_1 bands must be doubly degenerate. The effective Hamiltonian based on $\boldsymbol{k}\cdot\boldsymbol{p}$ theory [10] is essentially a Taylor expansion in the wave vector k of the interaction between E_1 and H_1 bands. The states are expressed in the basis $\{|E_1+; m_J = 1/2\rangle, |H_1+; m_J = 3/2\rangle, |E_1-; m_J = -1/2\rangle, |H_1-; m_J = -3/2\rangle\}$, where $|E_1\pm\rangle$ and $|H_1\pm\rangle$ are two states of Kramers' partners and $\pm$ represents spin-up/down. $|E_1\pm\rangle$ (odd) and $|H_1\pm\rangle$ (even) states have opposite parity under the 2D spatial reflection, hence the Hamiltonian matrix element connecting them must be odd under parity. Thus, to the lowest order of in-plane momentum k, $(|E_1+\rangle, |H_1+\rangle)$ and $(|E_1-\rangle, |H_1-\rangle)$ will each couple via a term linear in k. Moreover, $|E_1\pm\rangle$ and $|H_1\pm\rangle$ have angular momentum projections $m_J = \pm 1/2$ and $m_J = \pm 3/2$, respectively. This linear term must be proportional to $k_\pm = k_x \pm {\rm i}k_y$, to preserve the rotation symmetry around the QW growth axis z. On the other hand, the only terms allowed in the diagonal elements that connect states with the same parity have even powers of k including terms independent of k. Due to the coexistence of TRS and inversion symmetry, the subband must come in degenerate pairs at each k, so there exists no matrix element between the + state and the − state for the same band. Finally, if there are nonzero elements between $|E_1+\rangle$ and $|H_1-\rangle$ or $|E_1-\rangle$ and $|H_1+\rangle$, this would induce a higher order process coupling between the $\pm$ states of the same band and split the degeneracy. Therefore, these matrix elements are forbidden as well. From these simple symmetry considerations the following (BHZ) model was derived.

$$H(k) = \epsilon(k)\mathbb{I}_{4\times4} + \begin{pmatrix} M(k) & Ak_+ & 0 & 0 \\ Ak_- & -M(k) & 0 & 0 \\ 0 & 0 & M(k) & -Ak_- \\ 0 & 0 & -Ak_+ & -M(k) \end{pmatrix}, \tag{1}$$

where $\mathbb{I}_{4\times4}$ is the 4×4 identity matrix, and

$$\epsilon(\boldsymbol{k}) = C - D(k_x^2 + k_y^2),$$
$$M(\boldsymbol{k}) = M - B(k_x^2 + k_y^2), \tag{2}$$

where A, B, C, D, M are material parameters that depend on the QW geometry, which can be obtained by fitting the *ab initio* calculation and experimental data. From equation (1) we can find that the energy gap between the bands is $2M$, and B, typically negative, describes the curvature of the bands; A incorporates interband coupling to the lowest order. For $M/B < 0$, the eigenstates of the model describe a trivial insulator. But for thick QWs, the bands are inverted, M becomes negative, and the solution yields the topological edge states [2].

The existence of topologically protected edge states is an important property of the 2D TI. The edge states can be obtained by solving the BHZ model equation (1) with an open boundary condition. For example, consider the model Hamiltonian equation (1) defined on the half-space $x > 0$ in the xy plane. The effective Hamiltonian for the helical edge states can be derived (e.g. see [2]) as

$$H_{\rm edge} = Ak_y\sigma^z. \tag{3}$$

For HgTe QWs, it is found that $A \simeq 3.6\,{\rm eV\,Å}$ [9] and the Dirac velocity of the edge states is given by $v = A/\hbar \simeq 5.5\times10^5\,{\rm m\,s^{-1}}$. This analytical calculation can be confirmed by exact numerical diagonalization of the regularized Hamiltonian equation (1) on a strip of finite width [1], as shown in figure 3.

From the band structure (figure 3) and the effective Hamiltonian equation (3), we can see some novel properties of 2D TIs. The 2D TI or QSH insulator has an energy gap in the 2D bulk, but has metallic edge states bridging the bulk gap. At a given edge two edge states counter-propagate and have opposite spin polarization [5, 11, 12]. Thus, they are also called helical edge states for the locking between the spin and direction of motion [11]. TRS requires that the single-particle eigenstates for the electron must come with a degenerate time-reversed partner by Kramers' theorem. This implies that two edge states in a Kramers' pair have to cross each other at time-reversal-invariant momenta (TRIM) of the Brillouin zone, such as the Γ point. This degeneracy cannot be lifted to open a gap by nonmagnetic impurities or weak disorder without violating the TRS. Because of the mandatory crossing of the edge state levels described above, the 2D TI cannot be smoothly deformed into a gapped topological trivial insulator without helical edge states. This reveals the topological protection by TRS. Furthermore, the helicity of edge states can prevent backscattering. Since a pair of counter-propagating modes have opposite spin, an electron cannot be scattered from the forward-mover to the backward-mover without reversing its spin. In this way, TRS guarantees the robustness of topological edge states. The absence of backscattering is responsible for dissipationless transport along the edge. It should be noted that the above physical pictures only applies to the case of a single pair of helical edge states [5, 11, 12]. If there are two

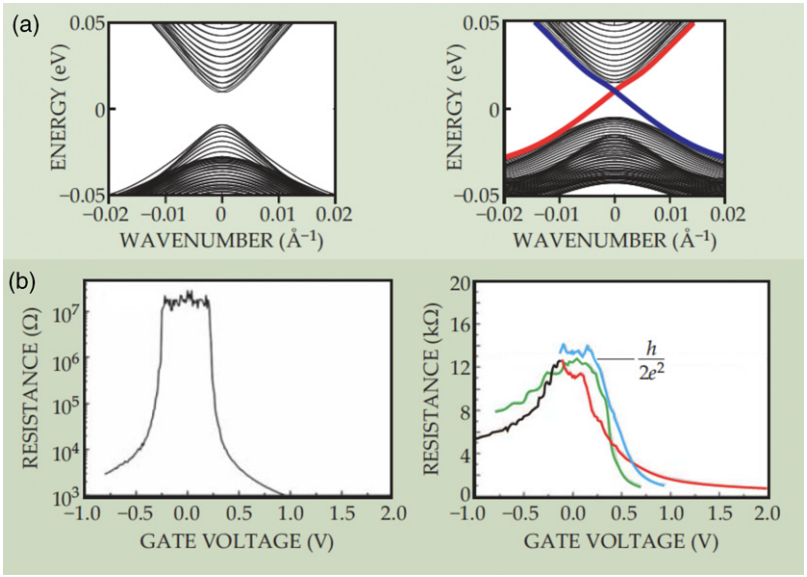

Figure 3. (*a*) Energy spectrum of the effective Hamiltonian equation (1). In a thin QW (left), there is a gap between the conduction band and the valence band. In a thick QW (right) there are gapless edge states on the left and right edges (red and blue lines, respectively). (*b*) Experimentally measured resistance of thin and thick QWs, plotted against the voltage applied to a gate electrode to change the chemical potential. The thin QW has nearly infinite resistance within the gap, whereas the thick QW has a quantized resistance plateau at $R = h/2e^2$, due to the perfectly conducting edge states. Moreover, the resistance plateau is the same for samples with different widths, from 0.5 μm (red) to 1.0 μm (blue), proof that only the edges are conducting. Adapted with permission from [1]. Copyright 2010 American Physical Society.

forward-movers and two backward-movers at a given edge, the forward-moving electron can be scattered to a backward channel without breaking the TRS. Such backscattering causes dissipation. Therefore, the edge states must consist of an odd number of forward- and backward-moving pairs. This even–odd effect becomes the key reason why the QSH insulator is characterized by a $\mathbb{Z}_2$ topological quantum invariant [5, 11, 12].

2.2. Realistic tight-binding calculations

The BHZ model above assumes inversion symmetry in HgTe for simplicity. Later calculations based on continuum models [9, 13], more realistic first-principles and tight-binding (TB) methods [14] have been carried out with full consideration of the bulk inversion asymmetry (BIA). They both confirmed the existence of the QSH state and the topological phase transition. Furthermore, the BIA term is found to play an important role in determining the spin orientation of the helical edge state. Here we mainly introduce the TB model results. Dai *et al* derived a TB Hamiltonian based on atomic orbitals and calculated the band structure for HgTe/CdTe QWs [14], in which their explicit atomic structure was considered. Band structure of QWs with increasing d_{QW} shows a clear quantum phase transition with a gap-closing and gap-reopening process, where E_1 and H_1 bands get inverted. Half-infinite QWs with a cutting edge along the y direction were calculated by the recursion method using the TB Hamiltonian, shown in figure 4. A single pair of helical edge states exist for thick QWs with $d_{\mathrm{QW}} > d_{\mathrm{c}}$. As shown in figure 4(*a*), these two states originate indeed from the edge, for their charge density is localized at the edge and decays rapidly into the bulk. The forward-mover is spin-up and the backward-mover is spin-down, carrying a spin current along the edge. Inside the QW energy gap, they cross each other at the Γ point. As the momentum k_y moves far away from Γ, they merge into the bulk bands. Therefore, the only low-energy states crossing the Fermi level inside the bulk gap are a single Kramers' pair of helical edge states. The first-principles and the TB model calculations agree well with the analytical results based on the BHZ continuum model.

2.3. Transport experiments

Less than one year after the theoretical prediction, Molenkamp and his colleagues observed the QSH state in HgTe/CdTe QWs grown by molecular-beam epitaxy (MBE) [8]. The existence of edge states is one of the most convincing ways to distinguish the QSH insulator from the trivial insulator. A simple method is to measure the longitudinal conductance on a strip of QW with finite width. A strip has two edges and the BHZ model predicts a helical state pair at each edge, hence we have two forward-moving states along the strip. Since each state is known to contribute a quantum conductance e^2/h, we expect a longitudinal conductance $2e^2/h$, corresponding to a resistance $h/2e^2$. Because of the suppression of backscattering, it is possible to reach perfect conductance, which is independent of the sample width and length. In order to see the phase transition from a trivial insulator to a QSH insulator, QW samples with d_{QW} ranging from 4.5 to 12.0 nm were grown [8, 9, 15]. These samples used in the transport measurement had very high mobilities of several 10^5 cm^2 V^{-1} s^{-1} and very low bulk carrier density $n < 5 \times 10^{11}$ cm^{-2}. A gate was applied to tune the chemical potential through the bulk energy gap when the resistance was measured. Figures 3(*c*) and (*d*) show the experimentally measured resistance for thin (4.5 nm) and thick QWs. The thin QW has a nearly zero conductance

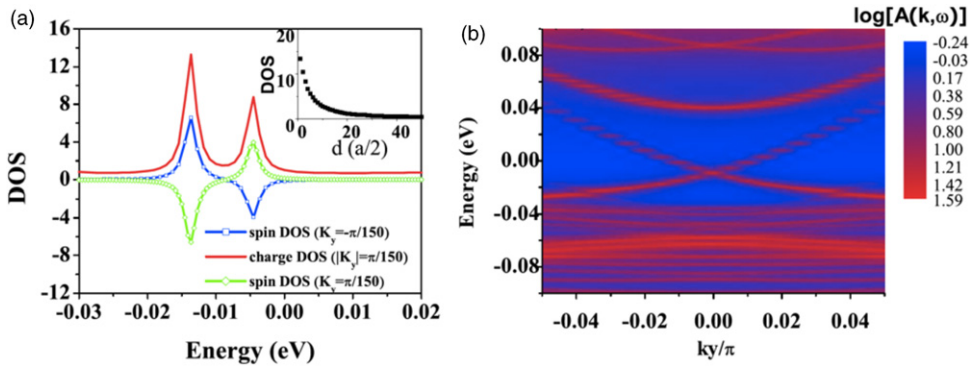

Figure 4. Realistic TB calculations of HgTe/CdTe QWs. (*a*) The spin density of states at the edge of the QW with thickness $d = 20$ monolayers (MLs). Here 1 ML contains 1 Hg and 1 Te with thickness $a/2$, where a is the lattice constant. In this work 20 ML thickness corresponds to a QSH state with inverted band structure. The inset plot shows the decay of the charge density for the edge state at the Γ point ($k_y = 0$). (*b*) The intensity color plot on the energy–momentum plane for the density of states at the edge of the QW with thickness $d = 20$ MLs. A single pair of helical edge states can be found in the bulk gap. The logarithm of the intensity was taken so that nonzero intensity clearly stands out. Adapted with permission from [14]. Copyright 2008 American Physical Society.

(infinite resistance) when the Fermi level lies inside the energy gap. In contrast, thick QWs have a quantized conductance $2e^2/h$ with a resistance plateau $R = h/2e^2$. This residual conductance is independent of the QW width, indicating its origin from the perfect-conducting edge states. Furthermore, it is found to be strongly influenced by TRS breaking due to an external magnetic field. The critical QW thickness for the topological quantum phase transition is around 6.3 nm, which agrees well with the prediction from the BHZ model. Further measurements [16] reported unique nonlocal transport properties related to the dissipationless transport of the helical edge states.

3. Three-dimensional topological insulators: Bi_2Se_3 family

Using the model Hamiltonian for the 2D TI HgTe QWs as a basic template, a simple but realistic model Hamiltonian of 3D TI can be derived for a class of materials, Bi_2Se_3, Bi_2Te_3 and Sb_2Te_3 [17, 18]. In these materials, a band inversion driven by SOC occurs at the Γ point. Different from bulk HgTe, their bulk states are fully gapped. The bulk gap is bridged by topologically protected surface states consisting of a single massless Dirac fermion. This 2D Dirac fermion is 'helical', i.e. the electron spin points perpendicular to the momentum, forming a left-hand helical texture in momentum space. Time-reversal (TR) invariant perturbation cannot introduce a gap for the surface state. But TR breaking perturbations on the surface can open a gap, leading to a novel topological magnetoelectric effect [19–21]. After the theoretical prediction of the 3D TI in Bi_2Te_3, Sb_2Te_3 [17] and Bi_2Se_3 [17, 22] class of materials, surface states with a single Dirac cone [22–24] were observed in angle-resolved photoemission spectroscopy (ARPES) experiments. Furthermore, spin-resolved ARPES measurements indeed observed the left-handed helical spin texture of the Dirac cone [25]. These pioneering theoretical and experimental works inspired much of the subsequent developments.

3.1. *Effective model Hamiltonian*

Bi_2Se_3, Bi_2Te_3 and Sb_2Te_3 crystallize in the same rhombohedral structure with space group D^5_{3d} ($R\bar{3}m$) and have five atoms in the primitive unit cell. The crystal structure of Bi_2Se_3 is shown as an example in figure 5(*a*), and consists of a layered structure where individual layers form a hexagonal lattice. The important symmetry axes are a trigonal axis (three-fold rotation symmetry) defined as the z-axis, a binary axis (two-fold rotation symmetry) defined as the x-axis and a bisectrix axis (in the reflection plane) defined as the y-axis. The material consists of five-atom layers stacked along the z direction, and is referred to as a quintuple layer (QL). Each QL consists of five atoms per unit cell with two equivalent Se atoms denoted by Se1 and Se1′, two equivalent Bi atoms denoted by Bi1 and Bi1′, and a third Se atom denoted by Se2 in figure 5(*b*). The coupling between two atomic layers within a QL is by strong chemical binding, while that between QLs is much weaker, and is predominantly of the van der Waals type. The primitive lattice vectors $\boldsymbol{t}_{1,2,3}$ and rhombohedral primitive unit cells are shown in figure 5(*a*). The Se2 site plays the role of an inversion center. Under inversion, Bi1 is mapped to Bi1′ and Se1 is mapped to Se1′. The existence of inversion symmetry enables us to construct eigenstates with definite parity for this system.

In order to have a better understanding of the band structure and orbitals involved, we start from the atomic energy levels and then consider the effects of crystal field splitting and SOC on the energy eigenvalues. This is summarized schematically in three stages: (I) chemical bonding, (II) crystal field splitting and (III) SOC (figure 6(*a*)). Since the states near the Fermi level are primarily from p-orbitals, we neglect the s-orbitals and start from the atomic p-orbitals of Bi (electronic configuration $6s^26p^3$) and Se ($4s^24p^4$). In stage (I), we consider chemical bonding between Bi and Se atoms within a QL, which corresponds to the largest energy scale in this problem. First, the formation of chemical bonds hybridizes the states of the Bi and Se atoms, pushing down all the Se states and lifting all the Bi states. Thereby we can construct the valence bands only from Se-p orbitals and conduction bands only from Bi-p orbitals. In a single unit cell of a QL, we can recombine

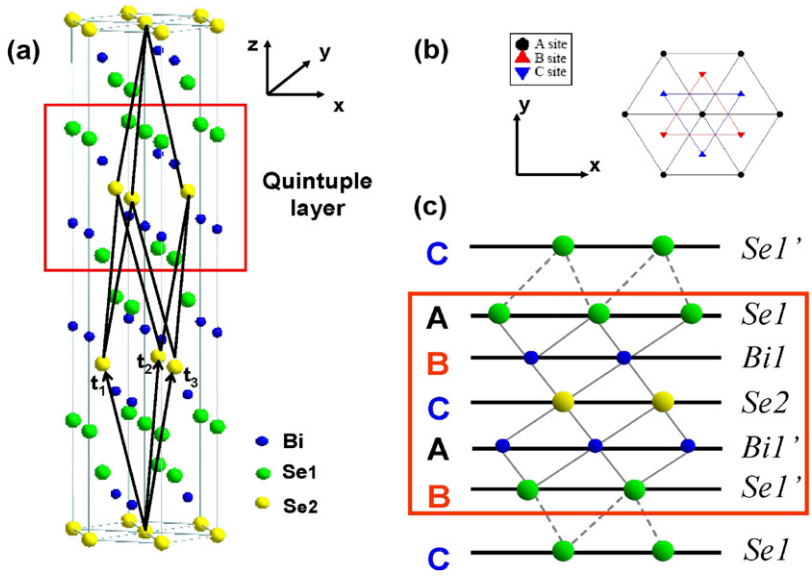

Figure 5. (*a*) Crystal structure of Bi_2Se_3 with three primitive lattice vectors denoted by $\boldsymbol{t}_{1,2,3}$. A QL with Se1-Bi1-Se2-Bi1′-Se1′ is indicated by the red box. (*b*) Top view along the z direction. Triangular lattice in one QL has three inequivalent positions, denoted by A, B and C. (*c*) Side view of the QL structure. Along the z direction, Se and Bi atomic layers are stacked in the sequence $\cdots$-C(Se1′)–A(Se1)–B(Bi1)-C(Se2)–A(Bi1′)–B(Se1′)–C(Se1)-$\cdots$. The Se1 (Bi1) layer is related to the Se1′ (Bi1′) layer by inversion,where Se2 atoms play the role of inversion center. Adapted with permission from [17]. Copyright 2009 Nature Publishing Group.

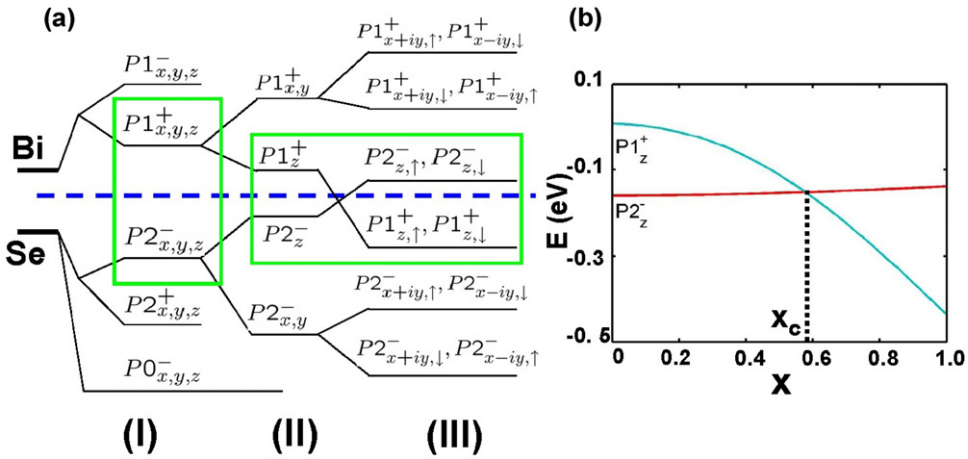

Figure 6. (*a*) Schematic picture of the evolution from the atomic $p_{x,y,z}$ orbitals of Bi and Se into the conduction and valence bands of Bi_2Se_3 at the Γ point. The three different stages (I), (II) and (III) represent the effect of turning on chemical bonding, crystal field splitting and SOC, respectively (see text). The blue dashed line represents the Fermi energy. (*b*) The energy levels $|P1^+_z\rangle$ and $|P2^-_z\rangle$ of Bi_2Se_3 at the Γ point versus an artificially rescaled atomic SOC $\lambda(\mathrm{Bi}) = x\lambda_0(\mathrm{Bi}) = 1.25x$ (eV), $\lambda(\mathrm{Se}) = x\lambda_0(\mathrm{Se}) = 0.22x$ (eV) (see text). A level crossing occurs between these two states at $x = x_c \simeq 0.6$. Adapted with permission from [17]. Copyright 2009 Nature Publishing Group.

these p-orbitals according to their parity. For valence bands, recombination results in three states (two odd, one even) from p-orbitals of three Se. For conduction bands, two states (one odd, one even) are derived from p-orbitals of two Bi. In figure 6(*a*), these five hybridized states are labeled $\left|P1^{\pm}_{x,y,z}\right\rangle$, $\left|P2^{\pm}_{x,y,z}\right\rangle$ and $\left|P0^{-}_{x,y,z}\right\rangle$, where the superscripts ± stand for the parity of the corresponding states. In stage (II), we consider the effect of crystal field splitting between different p-orbitals. According to the point group symmetry, the p_z orbital is split from the p_x and p_y orbitals while the latter two remain degenerate. After this splitting, the energy levels closest to the Fermi energy turn out to be the p_z levels $\left|P1^{+}_{z}\right\rangle$ and $\left|P2^{-}_{z}\right\rangle$. In the last stage (III), we take into account the effect of SOC. The atomic SOC Hamiltonian is given by $H_{\mathrm{SO}} = \lambda \boldsymbol{L}\cdot\boldsymbol{S}$, with $\boldsymbol{L}$, $\boldsymbol{S}$ the orbital and spin angular momenta, respectively, and λ the strength of SOC. The SOC Hamiltonian mixes spin and orbital angular momenta while preserving the total angular momentum. This leads to a level repulsion between $\left|P1^{+}_{z},\uparrow\right\rangle$ and $\left|P1^{+}_{x+iy},\downarrow\right\rangle$, and between similar combinations. Consequently, the energy of the $\left|P1^{+}_{z},\uparrow(\downarrow)\right\rangle$ state is pushed down by the effect of SOC, and the energy of the $\left|P2^{-}_{z},\uparrow(\downarrow)\right\rangle$ state is pushed up. If SOC is larger than a critical value $\lambda > \lambda_c$, the order of these two energy levels is reversed. To illustrate this inversion process explicitly, the energy levels $\left|P1^{+}_{z}\right\rangle$ and $\left|P2^{-}_{z}\right\rangle$ have been calculated [17] for a model Hamiltonian of Bi_2Se_3 with artificially rescaled atomic SOC parameters

$\lambda(\mathrm{Bi}) = x\lambda_0(\mathrm{Bi})$, $\lambda(\mathrm{Se}) = x\lambda_0(\mathrm{Se})$, as shown in figure 6(*b*). Here $\lambda_0(\mathrm{Bi}) = 1.25\,\mathrm{eV}$ and $\lambda_0(\mathrm{Se}) = 0.22\,\mathrm{eV}$ are the actual values of the SOC strength for Bi and Se atoms, respectively [26]. From figure 6(*b*), one can clearly see that a level crossing occurs between $|P1_z^+\rangle$ and $|P2_z^-\rangle$ when the SOC strength is about 60% of its actual value. Since these two levels have opposite parity, the inversion between them drives the system into a TI phase. Therefore, the mechanism for the occurrence of a 3D topological insulating phase in this system is closely analogous to the mechanism for the 2D QSH effect in HgTe [7]. More precisely, to determine whether or not an inversion-symmetric crystal is a TI, we must have full knowledge of the states at *all* of the eight TRIM [20]. At the same time *ab initio* calculations [17] of the parity of Bloch states at all TRIM have confirmed that the system is a (strong) TI (see the following section).

Since the topological nature is determined by the physics near the Γ point, it is possible to write down a simple effective Hamiltonian to characterize the low-energy, long-wavelength properties of the system [18]. Starting from the four low-lying states $|P1_z^+, \uparrow(\downarrow)\rangle$ and $|P2_z^-, \uparrow(\downarrow)\rangle$ at the Γ point, such a Hamiltonian can be constructed by the theory of invariants [27] at a finite wave vector $\boldsymbol{k}$. The important symmetries of the system are TR symmetry T, inversion symmetry I and three-fold rotation symmetry C_3 around the z-axis. In the basis $\{|P1_z^+, \uparrow\rangle, |P2_z^-, \uparrow\rangle, |P1_z^+, \downarrow\rangle, |P2_z^-, \downarrow\rangle\}$, the representation of these symmetry operations is given by $T = \mathrm{i}\sigma^y\mathcal{K} \otimes \mathbb{I}_{2\times2}$, $I = \mathbb{I}_{2\times2} \otimes \tau_3$ and $C_3 = \exp\left(\mathrm{i}\frac{\pi}{3}\sigma^z \otimes \mathbb{I}_{2\times2}\right)$, where $\mathbb{I}_{n\times n}$ is the $n \times n$ identity matrix, $\mathcal{K}$ is the complex conjugation operator and $\sigma^{x,y,z}$ and $\tau^{x,y,z}$ denote the Pauli matrices in the spin and orbital space, respectively. By requiring these three symmetries and keeping only terms up to quadratic order in $\boldsymbol{k}$, we obtain the following generic form of the effective Hamiltonian:

$$H(\boldsymbol{k}) = \epsilon_0(\boldsymbol{k})\mathbb{I}_{4\times4} + \begin{pmatrix} \mathcal{M}(\boldsymbol{k}) & A_1k_z & 0 & A_2k_- \\ A_1k_z & -\mathcal{M}(\boldsymbol{k}) & A_2k_- & 0 \\ 0 & A_2k_+ & \mathcal{M}(\boldsymbol{k}) & -A_1k_z \\ A_2k_+ & 0 & -A_1k_z & -\mathcal{M}(\boldsymbol{k}) \end{pmatrix}, \tag{4}$$

with $k_\pm = k_x \pm \mathrm{i}k_y$, $\epsilon_0(\boldsymbol{k}) = C + D_1k_z^2 + D_2k_\perp^2$ and $\mathcal{M}(\boldsymbol{k}) = M - B_1k_z^2 - B_2k_\perp^2$. The parameters in the effective model can be determined by fitting the energy spectrum of the effective Hamiltonian to that of *ab initio* calculations [17, 18, 28].

Except for the identity term $\epsilon_0(\boldsymbol{k})$, the Hamiltonian equation (4) is similar to the 3D Dirac model with uniaxial anisotropy along the z direction, but with the crucial difference that the mass term is $\boldsymbol{k}$-dependent. From the fact that $M, B_1, B_2 > 0$ we can see that the order of the bands $|P1_z^+, \uparrow(\downarrow)\rangle$ and $|P2_z^-, \uparrow(\downarrow)\rangle$ is inverted around $\boldsymbol{k} = 0$ compared with large $\boldsymbol{k}$, which correctly characterizes the topologically nontrivial nature of the system. In addition, the Dirac mass M, i.e. the bulk insulating gap, is ∼0.3 eV, which allows the possibility of having a room-temperature TI. Such an effective model can be used for further theoretical study of the Bi_2Se_3 system, as far as low-energy properties are concerned.

The existence of topological surface states is one of the most important properties of TIs. In analogy to the 2D QSH case (BHZ model), the surface effective model can be obtained by projecting the bulk Hamiltonian onto the surface states. To leading order in k_x, k_y, the effective surface Hamiltonian H_{surf} has the following matrix form [17, 18]:

$$H_{\mathrm{surf}}(k_x, k_y) = C + A_2\left(\sigma^x k_y - \sigma^y k_x\right) = C + A_2(\hat{\boldsymbol{z}} \times \boldsymbol{\sigma}) \cdot \boldsymbol{k}. \tag{5}$$

For fitting parameter $A_2 = 4.1\,\mathrm{eV\,Å}$, the velocity of the surface states is given by $v = A_2/\hbar \simeq 6.2 \times 10^5\,\mathrm{m\,s^{-1}}$, which agrees reasonably with *ab initio* results (see figure 8) $v \simeq 5.0 \times 10^5\,\mathrm{m\,s^{-1}}$. It should be noted that the Pauli $\boldsymbol{\sigma}$ matrix in the model Hamiltonian equation (5) is proportional to the physical spin. Therefore, in Bi_2Se_3 family materials, the upper Dirac cone has a left-hand helicity when looking from above the surface (figure 8).

Corrections to the effective Hamiltonian equation (4) that are of higher order in $\boldsymbol{k}$ can also be considered. To cubic (k^3) order, some new terms can break the continuous rotation symmetry around the z-axis to a discrete three-fold rotation symmetry C_3. Correspondingly, the Fermi surface (FS) of the surface state acquires a hexagonal shape [29], which leads to important consequences for experiments on TIs such as surface-state quasiparticle interference [30–33]. A modified version of the effective model equation (4) taking into account corrections up to k^3 has been obtained for the three TIs Bi_2Se_3, Bi_2Te_3 and Sb_2Te_3 based on *ab initio* calculations [18]. In this same work [18], an eight-band model is also proposed for a more quantitative description of this family of TIs.

3.2. *Ab initio calculations*

The guiding principle of using 'inverted' band structure to look for 2D TI HgTe QWs can also be generalized to other 2D and 3D systems. The recipe is to search for insulators where the conduction band and the valence band have opposite parity, and a 'band inversion' occurs when SOC is turned on. The existence of band inversion as well as the parity can be obtained directly from band structure calculations. *Ab initio* calculations were carried out for Bi_2Se_3, Bi_2Te_3, Sb_2Se_3 and Sb_2Te_3 [17]. A density-functional method introduced into the BSTATE package [34] was employed with the Perdew–Burke–Ernzerhof-type (PBE) generalized gradient approximation (GGA) [35].

The calculated BB structures are shown in figure 7. In the following we take Bi_2Se_3 for example. It has an energy gap of about 0.3 eV. By comparing the band structure without SOC (figure 7(*a*)) and with SOC (figure 7(*b*)), one can clearly see that a qualitative change induced by turning on SOC is an anti-crossing feature around the Γ point. It thus indicates an inversion between the conduction band and valence band due to SOC effects, suggesting that Bi_2Se_3 is a TI. To firmly establish the topological nature of this material, the parity criteria proposed by Fu and Kane [20] were adopted by checking the parity of Bloch states at all TRIM for all valence bands. Thus, the product of the parities of the Bloch wavefunction was calculated for the occupied bands at all TRIM Γ, F, L, Z in the Brillouin zone. As expected, it is found that at the Γ point, the parity of one occupied band is changed when SOC is turned on,

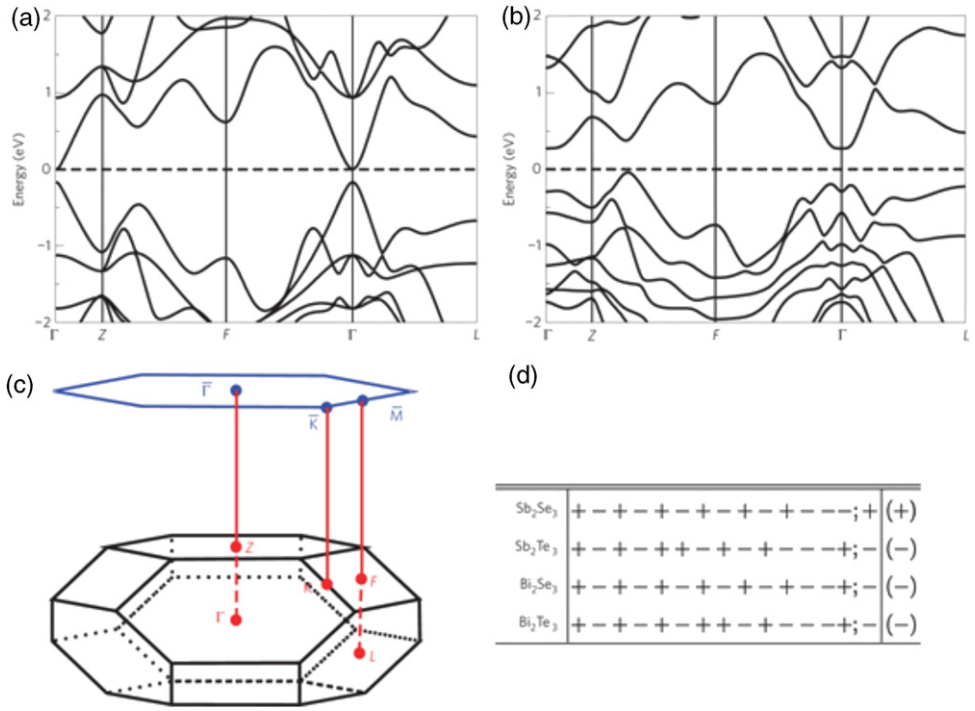

Figure 7. *Ab initio* calculated BB structure for Bi_2Se_3 without (*a*) and with (*b*) SOC. The dashed line indicates the Fermi level. (*c*) Brillouin zone for Bi_2Se_3 with space group $R\bar{3}m$. The four inequivalent TR-invariant points are $\Gamma(0, 0, 0)$, $L(0.5, 0, 0)$, $F(0.5, 0.5, 0)$ and $Z(0.5, 0.5, 0.5)$ in units of reciprocal lattice vectors. The blue hexagon shows the 2D Brillouin zone of the projected (1, 1, 1) surface, in which the high-symmetry k points $\bar{\Gamma}$, $\bar{M}$ and $\bar{K}$ are labeled. (*d*) The parity of the band at the Γ point for the four materials Sb_2Te_3, Sb_2Se_3, Bi_2Se_3 and Bi_2Te_3. Here, the parities of fourteen occupied bands are shown, including five s bands and nine p bands, and the lowest unoccupied band. The product of the parities for the fourteen occupied bands is given in brackets on the right of each row. Adapted with permission from [17]. Copyright 2009 Nature Publishing Group.

whereas the parity remains unchanged for all occupied bands at the other momenta F, L, Z. As the system without SOC is guaranteed to be a trivial insulator, Bi_2Se_3 is concluded to be a strong TI. The same calculation was carried out for three other materials, among which Sb_2Te_3 and Bi_2Te_3 are also strong TIs and Sb_2Se_3 is a trivial insulator. The parity eigenvalues of the highest 14 bands below the Fermi level and the first conduction band at the Γ point are listed in figure 7(*d*). From this table we can see that the product of parities of occupied bands at the Γ point changes from the trivial material Sb_2Se_3 to the three non-trivial materials, owing to an exchange of the highest occupied state and the lowest unoccupied state. This agrees with the earlier analysis that an inversion between the conduction band and valence band occurs at the Γ point.

The topological feature can also be demonstrated directly from the surface state calculations. The surface states of these four systems were calculated on the basis of an *ab initio* calculation. The maximally localized Wannier function (MLWF) constructed from an *ab initio* calculation [36, 37] offers an advantage to calculate the surface states on a semi-infinite surface. The semi-infinite system can be divided into a surface slab with finite thickness and the remaining part as the bulk. The MLWF hopping parameters for the bulk part can be constructed from the bulk *ab initio* calculation, and the ones for the surface slab can be constructed from the *ab initio* calculation of the slab, in which the surface corrections to the lattice constants and band structure have been considered self-consistently and the chemical potential is determined by the charge neutrality condition. With these bulk and surface MLWF hopping parameters, the surface Green's function of the semi-infinite system was obtained through an iterative method [38, 39]. The imaginary part of the surface Green's function is the local density of states (LDOS), from which the dispersion of the surface states can be obtained. The surface LDOS on the [1 1 1] surface for all four systems is shown in figure 8. For Sb_2Te_3, Bi_2Se_3 and Bi_2Te_3, one can clearly see the topological surface states that form a single Dirac cone at the point. In comparison, Sb_2Se_3 has no surface state and is a topologically trivial insulator. Thus, the surface-state calculation agrees well with the bulk parity analysis, and confirms conclusively the topologically nontrivial nature of the three materials. For Bi_2Se_3, the Fermi velocity of the topological surface states is $v_F \simeq 5.0 \times 10^5\ \mathrm{m\,s^{-1}}$, which is similar to that of the other two materials.

It should be noted that the surface-state calculation is not limited to the MLWF method. State-of-the-art first-principles calculations including SOC can also give the surface band structure by a slab model setup [28, 40]. Calculation shows that the penetration depth of the surface state into the bulk is about 2–3 QLs, i.e. 2–3 nm [28]. Therefore, a slab of 5 or 6 QLs can simulate a surface by suppressing the interaction between top and bottom surfaces. Interestingly, in a thin film this interaction between top and bottom surface states can open a new energy gap at the Dirac point and the thin film becomes a 2D insulator. When the VBM and CBM ordering gets inverted at proper thickness, the thin film is predicted to become a 2D TI [40, 41].

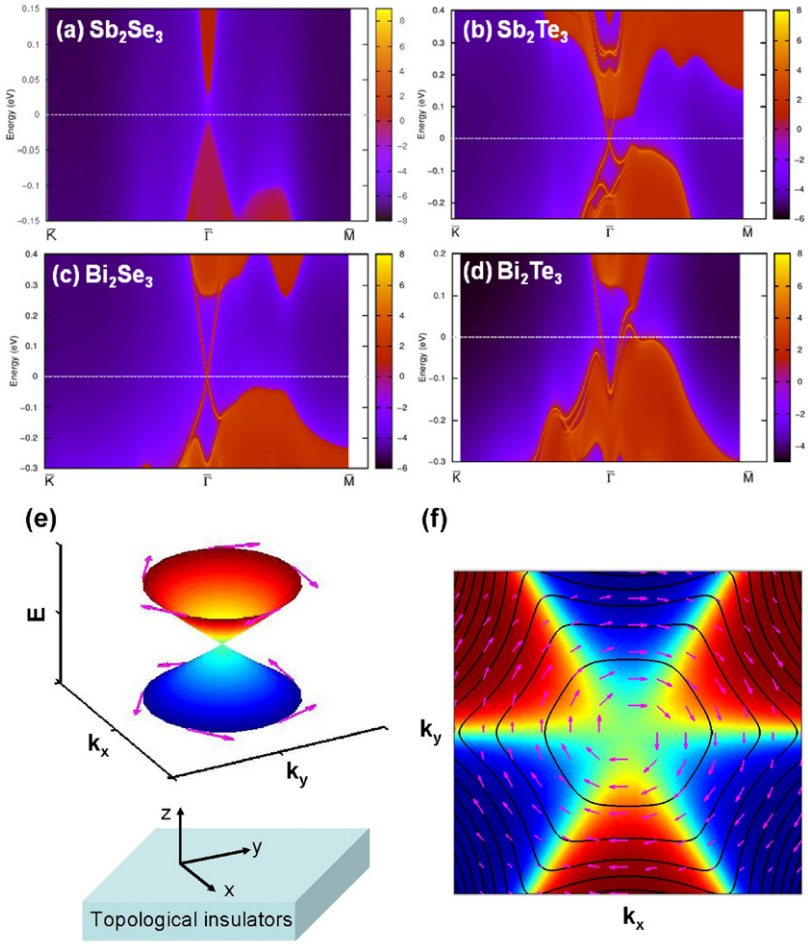

Figure 8. (*a*)–(*d*) Energy and momentum dependence of the LDOS for the Bi_2Se_3 family of materials on the [1 1 1] surface. A warmer color represents a higher LDOS. Red regions indicate bulk energy bands and blue regions indicate a bulk energy gap. The surface states can be clearly seen around the Γ point as red lines dispersing inside the bulk gap. (*e*) Spin polarization of the surface states on the top surface, where the *z* direction is the surface normal, pointing outward. Adapted with permission from [17, 18]. Copyright 2009 Nature Publishing Group and 2010 American Physical Society, respectively.

3.3. ARPES experiments

ARPES experiments are uniquely positioned to detect the topological surface states. ARPES experiments on Bi_2Se_3 [22] and Bi_2Te_3 [23, 24] reported a remarkably simple surface-state spectrum with a single Dirac cone located at the $\bar{\Gamma}$ point and a large bulk energy gap, in accordance with theoretical predictions. For Bi_2Se_3, a single Dirac cone with linear dispersion is clearly observed at the $\bar{\Gamma}$ point within the band gap. Spin-resolved ARPES [25] measured the opposite spin polarization for opposite $\boldsymbol{k}$, thereby indicating the helical nature of the spin polarization for surface states.

As discussed above, Bi_2Se_3 has a finite density of n-type carriers due to intrinsic doping. Therefore, the above ARPES data show that the Fermi level lies above the conduction band bottom and the sample is, in fact, a metal rather than an insulator in the bulk. To obtain a true topologically insulating state with the Fermi energy tuned into the bulk gap, careful control of external doping is required. Such control was first reported by Chen *et al* (figure 9) for a sample of Bi_2Te_3 with 0.67% Sn doping [23]. Some recent work on Sb_2Te_3 [24] supports the theoretical prediction that this material is also a TI [17]. This family of materials is moving to the forefront of research on TIs due to the large bulk gap and the simplicity of the surface-state spectrum. Although the simple model equation (5) captures most of the surface-state physics of these systems, experiments report a hexagonal surface-state FS (see figure 9). This hexagonal wrapping effect can be easily taken into account by including an additional k^3 term in the surface Hamiltonian equation (5) [29] (see section 3.1).

In addition to the bulk crystalline samples, thin films of Bi_2Se_3 and Bi_2Te_3 [42–44] were also characterized by ARPES. The thin films were grown to initiate a study of the crossover from a 3D TI to a 2D TI [40, 41].

4. Other materials

4.1. $Bi_{1-x}Sb_x$ alloy

4.1.1. Theoretical prediction. $Bi_{1-x}Sb_x$ has a complicated electronic structure which cannot be easily captured by a simple analytical model, as performed in the two previous examples. To determine the topological $\mathbb{Z}_2$ invariant for a generic band structure, Fu and Kane derived a simple method

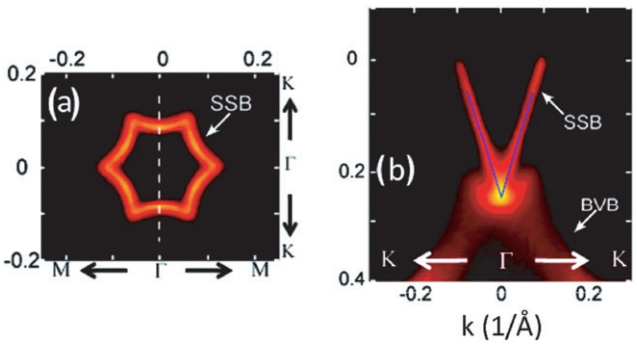

Figure 9. ARPES measurement of (a) shape of the FS and (b) band dispersion along the K–Γ–K direction, for Bi_2Te_3 nominally doped with 0.67% Sn. Adapted with permission from [23]. Copyright 2009 American Association for the Advancement of Science.

for materials with inversion symmetry [20]. Using this method they predicted the first 3D TI $Bi_{1-x}Sb_x$ alloy with composition x in a certain range that was soon observed by ARPES experiments [45]. This simple method using the parity of single particle states was later extensively employed in band structure calculations to identify new topological materials.

When inversion symmetry is present, the parity ξ of single particle states is well defined. Using the parity, a quantity can be defined at the TRIM Γ_i as,

$$\delta_i = \prod_{m=1}^{N} \xi_{2m}(\Gamma_i). \tag{6}$$

Here $\xi_{2m}(\Gamma_i) = \pm 1$ is the parity eigenvalue of the $2m$th occupied energy band at Γ_i, which shares the same eigenvalue $\xi_{2m} = \xi_{2m-1}$ with its degenerate Kramers' partner [20]. Using δ_i, the $\mathbb{Z}_2$ invariant ν_{2D} for 2D TI can be defined as

$$(-1)^{\nu_{2D}} = \prod_{i=1}^{4} \delta_i, \tag{7}$$

where $i = 1, 2, 3, 4$ labels the four TRIM in the 2D Brillouin zone. $(-1)^{\nu_{2D}} = +1$ implies a trivial insulator while $(-1)^{\nu_{2D}} = -1$ implies a TI. The 3D (strong) topological invariant is naturally defined as [20, 46]

$$(-1)^{\nu_{3D}} = \prod_{i=1}^{8} \delta_i. \tag{8}$$

In addition to the strong invariant ν_{3D}, three additional invariants in 3D ($\nu_1\nu_2\nu_3$) can be defined as weak topological invariants [20, 46–48]. These $\mathbb{Z}_2$ invariants can be arranged as a 3D vector with elements ν_k given by

$$(-1)^{\nu_k} = \prod_{n_k=1; n_{j\neq k}=0,1} \delta_{i=(n_1 n_2 n_3)}, \tag{9}$$

where ($\nu_1\nu_2\nu_3$) depend on the choice of reciprocal lattice vectors and are only strictly well defined when a well-defined lattice is present. The above method uses only the bulk (2D or 3D) band structure without calculating the surface states.

The crystal structures of Bi and Sb are both of rhombohedral A7 type with space group $R\bar{3}m$ (similar to the Bi_2Se_3 family). The A7 structure can be viewed as a fcc NaCl structure distorted along the (1 1 1) direction. Triangular lattices in the (1 1 1) plane get paired and form bi-layers (BLs). The lattice structure is shown in figure 10(a). Both Bi and Sb have similar lattice parameters and share inversion symmetry. They form solid alloys $Bi_{1-x}Sb_x$ that have long been studied for their thermoelectric properties [51].

Pure Bi and Sb are group-V semimetals having a direct energy gap throughout the Brillouin zone but a negative indirect gap due to band overlap. Their schematic band structures are shown in figure 11. In Bi, the CBM and the VBM at the L point are derived from symmetric orbitals (L_s) with even parity and antisymmetric orbitals (L_a) with odd parity, respectively. Between them is a small energy gap. However, in Sb L_s and L_a are inverted. Due to existence of inversion symmetry and direct energy gap, the above parity criteria can be applied to determine their topological feature. Bi has $\delta_i = -1$ at all eight TRIM including 1Γ, 3L, 3X and 1T points and hence is trivial with $\mathbb{Z}_2$ invariants (0;000). But Sb has $\delta_i = +1$ at 3L points due to the $L_s - L_a$ inversion and $\delta_i = -1$ at all other TRIM, and is topologically nontrivial with $\mathbb{Z}_2$ (1;111). The idea is to combine them into an alloy to make a TI with both a full energy gap and a nontrivial $\mathbb{Z}_2$ invariant. When we dope Bi with increasing Sb composition x, there exist two main modifications to the band structure of Bi. First, the VBM at T is pushed below the CBM, resulting in a real insulator in a certain x range 0.07–0.22. Second, Sb dopants reduce the SOC in Bi and induce L_s and L_a band inversion after a critical x value 0.04. Subsequently $Bi_{1-x}Sb_x$ becomes a gapped TI with the $\mathbb{Z}_2$ invariant (1;111).

The surface states of $Bi_{1-x}Sb_x$ cannot be described by a simple Hamiltonian like equation (1) due to the complexity (see below). Following the prediction, band structure calculations using phenomenological tight-binding model by Teo *et al* [49] and the Wannier function method based on *ab initio* approaches by Zhang *et al* [50] have been performed for the (1 1 1) surface of $Bi_{1-x}Sb_x$ alloy. An important and useful feature to judge a TI is that an arbitrary energy level inside the bulk gap will be intersected by an odd number of surface bands between two TRIM [20]. Both calculations showed a consistent picture that an odd number of surface states cross the Fermi level between two TRIM, which confirms the alloy is a strong TI. As shown in figure 10, the TB band structure shows three surface bands crossing the Fermi energy between the $\bar{\Gamma}$ and $\bar{M}$ points inside the bulk gap, while the *ab initio* band structure shows five bands. By considering an additional trivial surface band hybridization, the latter can reproduce well the experimental results [45, 52]. The *ab initio* calculations [50] also gave the spin-resolved FSs and showed the vortex structures, which agree with experiments.

4.1.2. ARPES experiments. ARPES experiment by Hsieh *et al* [45] revealed the band structure on the (1 1 1) surface of $Bi_{0.9}Sb_{0.1}$. One can see that there are five bands crossing the Fermi energy in the bulk gap, in good accordance with *ab initio* calculations [50]. This provides evidence that $Bi_{1-x}Sb_x$ is a strong TI. Moreover, Hsieh *et al* [53]

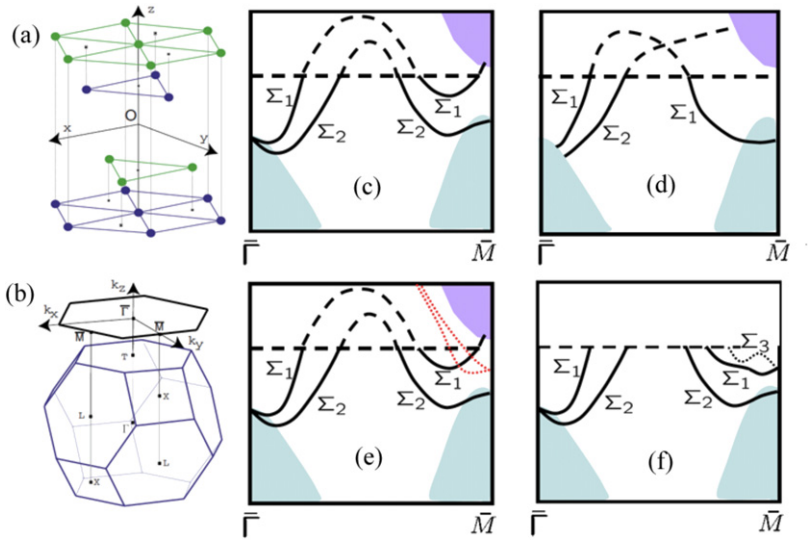

Figure 10. (*a*) Crystal structure and (*b*) 3D Brillouin zone and its projection onto the (1 1 1) surface (right). Adapted with permission from [49]. Copyright 2008 American Physical Society. (*c*)–(*f*) Schematic pictures for the comparison of the surface bands obtained from (*c*) *ab initio* calculation [50], (*d*) TB model [49] and (*f*) ARPES experiment results [45]. In the ARPES experiment, an additional Σ_3 surface band (dotted line in (*f*)) becomes degenerate with the Σ_1 band at the $\bar{M}$ point. This additional band may come from hybridization between the topological surface states and the other trivial surface states, as suggested by the red dotted line in (*e*). Adapted with permission from [50]. Copyright 2009 American Physical Society.

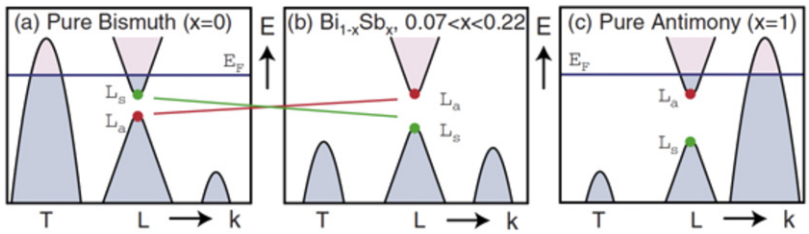

Figure 11. Schematic representation of the band structure of $Bi_{1-x}Sb_x$, which evolves from semimetallic behavior for $x < 0.07$ to semiconducting behavior for $0.07 < x < 0.22$ and back to semimetallic behavior for $x > 0.22$. The conduction and valence bands L_s, L_a invert at $x = 0.04$. Adapted with permission from [3]. Copyright 2010 American Physical Society.

measured the spin polarization of surface states using spin-resolved ARPES. On the FS, the spin is found to correlate with the momentum and rotate by 360°, resulting in a Berry phase π. The topological properties of $Bi_{1-x}Sb_x$ solid alloys and thin films were further investigated by recent experiments [52, 54–56].

4.2. Variations of HgTe family of materials

As we see in section 2, bulk HgTe has an inverted band structure between p-type Γ_8 and s-type Γ_6 bands. According to the parity criteria it is a strong TI. However, the bulk gap is zero, because the heavy hole (VBM) and light hole (CBM) are degenerate at Γ due to the cubic symmetry. There are two ways to open the energy gap. One is to fabricate HgTe QWs, where an energy gap opens and band inversion persists above a critical QW thickness. This is the 2D TI discussed earlier. The other is to break the cubic symmetry and to lift the heavy-hole and light-hole degeneracy, e.g. by applying strain, turning it into a 3D TI [14, 20]. Recent theoretical [14, 57] and experimental [58] works show that strained HgTe becomes a strong TI with topological surface states. On the other hand, many new materials with a similar band structure to HgTe are proposed to be TIs. Usually they have an inverted band structure but a zero energy gap induced by crystal symmetry. External strain or QW fabrication is required to open the energy gap and create a gapped TI. In this section, we focus on strained HgTe and related new HgTe-type topological materials.

4.2.1. Strained HgTe. Using the same TB model, which calculates the edge states of HgTe/CdTe QWs, Dai *et al* [14] performed surface-state calculations for strained HgTe and HgTe/CdTe interfaces. After applying uniaxial strain to the bulk, they demonstrated successfully that HgTe becomes a strong TI with helical surface states. Two surface states appear inside the bulk gap. They cross each other at the Brillouin zone boundary, $\bar{X}$ and $\bar{M}$. At the $\bar{\Gamma}$ point one merges into the bulk valence bands (BVBs) and the other into the conduction bands. But at the HgTe/CdTe interface a clear single Dirac cone from surface states is found at $\bar{\Gamma}$. Understanding the explicit energy dispersion of these surface states is crucial for experimental investigations on HgTe. Recently *ab initio* calculations have been carried out to study these surface states and the strain effect on the band structure. A new feature of the surface

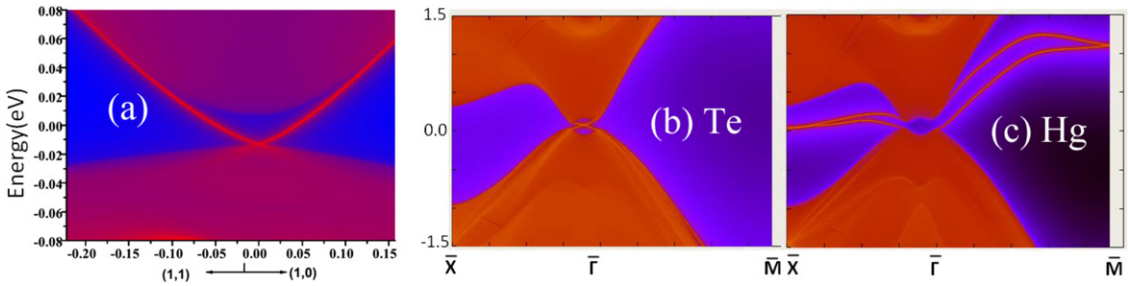

Figure 12. Calculated band structures for HgTe/CdTe interface and HgTe surfaces. (*a*) Tight-binding calculated surface states around $\bar{\Gamma}$ at the HgTe/CdTe interface. The uniaxial strain 2% is applied along the (0 0 1) direction by choosing the c/a ratio to be 0.98, and the HgTe/CdTe interface is chosen along the (0 0 1) direction. Adapted with permission from [14]. Copyright 2008 American Physical Society. *Ab initio* based MLWF calculated band structure for (*b*) Te and (*c*) Hg terminated HgTe (0 0 1) surface, where 5% uniaxial strain is applied along (0 0 1). For the Te terminated surface, a single Dirac cone is found at the $\bar{\Gamma}$ point, while the Dirac points exist at $\bar{X}$ and $\bar{M}$ for the Hg terminated surface. Adapted with permission from [57].

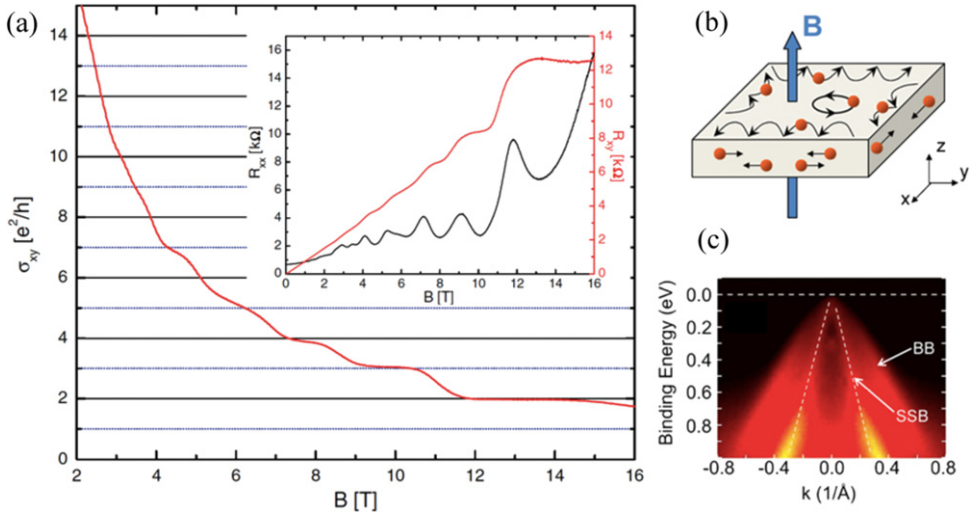

Figure 13. (*a*) Transport data on the strain-gapped 70 nm thick HgTe sample. The Hall conductivity measured at 50 mK shows plateaus at the quantized values. The inset shows the Hall resistance R_{xy}, together with the longitudinal resistance R_{xx}. (*b*) Schematic picture of the coexistence of the chiral edge states from the upper and lower surfaces and the nonchiral metallic modes at the side surfaces. The magnetic field is perpendicular to the upper and lower surfaces but parallel to the four side surfaces. (*c*) ARPES measurements on a relaxed, 1 μm thick HgTe sample. The dispersion of the surface state band (SSB) and BBs is indicated by arrows. Adapted with permission from [58]. Copyright 2011 American Physical Society.

states was found in which their energy dispersion depends sensitively on the surface local environment. The topological surface states can vary energetically, though their topological nature is not sensitive to the detailed surface condition. On the (0 0 1) surface of HgTe, the outmost atomic layer can be either a Hg or a Te layer. For a Hg layer terminated surface, two surface states cross at $2\bar{X}$ and $1\bar{M}$ and form three Dirac cones in the Brillouin zone, similar to the result of Dai *et al*. However, only a single Dirac point at $\bar{\Gamma}$ is found for the Te terminated surface, as shown in figure 12. In addition, a single Dirac cone at $\bar{\Gamma}$ point was found on the HgTe/CdTe interface. This can be understood by the fact that the HgTe/CdTe interface is very close to a Te terminated surface. From a practical experimental viewpoint, the bulk energy gap dependence on the uniaxial strain was investigated. It was found that even small compressive strain (e.g. 1.3% uniaxial strain, 0.3 GPa pressure) can open a gap comparable to the room temperature one. Therefore, the strained HgTe can become a room temperature 3D TI under ambient pressure.

Molenkamp and colleagues [58] performed transport measurements on a 70 nm thick HgTe film grown by MBE on a CdTe substrate. Because CdTe has 0.3% lattice mismatch with HgTe, in-plane strain is introduced into the HgTe layer. Under this strain the bulk energy gap is estimated to be ∼22 meV. The surface-state width is around 2–3 nm and hence hybridization between top (vacuum) and bottom (CdTe interface) surfaces can be neglected in the 70 nm thick film. Therefore, this film can safely be regarded as a 3D material. Their samples have quite low bulk carrier density and reach the bulk insulating regime (intrinsic TI) at a low temperature, which guarantees the successful observation of the quantum Hall effect (QHE) from the topological surface states. In contrast, the mostly studied Bi_2Se_3 types of materials have strong defect doping and lower carrier mobility, which hinders the surface transport measurements.

The transport data from QHE are shown in figure 13. The QHE in 2D-Dirac like topological surface states is conclusively demonstrated. Compared with an ordinary 2D electron system,

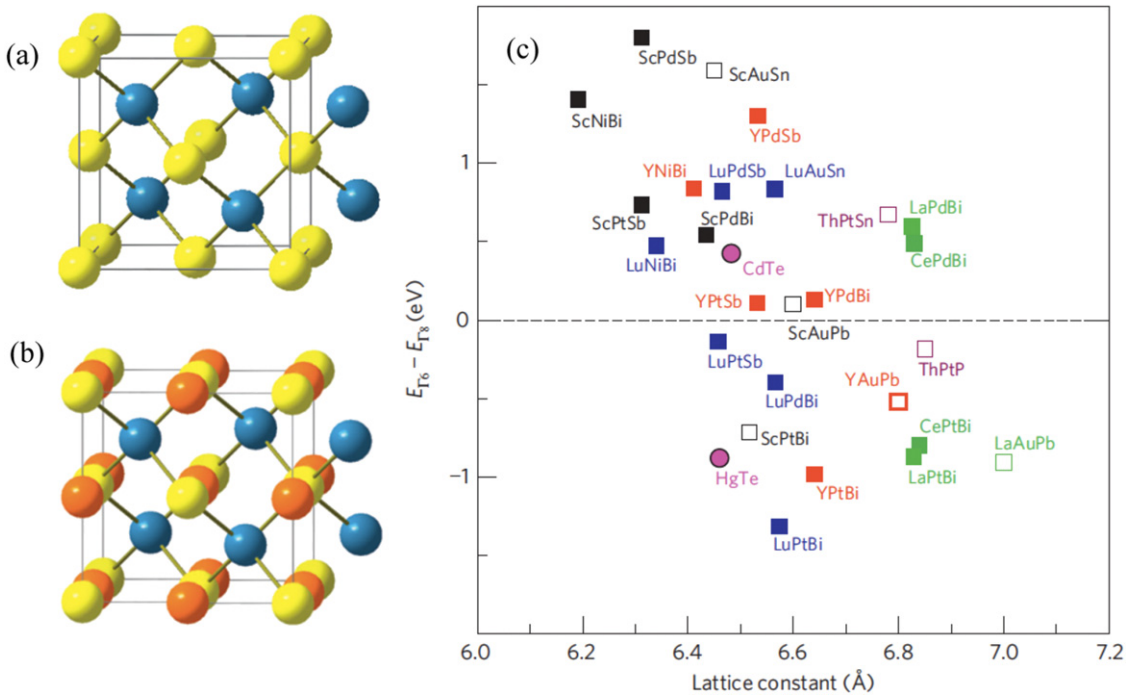

Figure 14. Comparison of (a) the zinc-blende and (b) the half-Heusler (XYZ) $C1_b$ crystal structure. The zinc-blende (YZ) structure is shown on the left, and the $C1_b$ (XYZ) on the right. Yellow and blue spheres correspond to the main group (Z) and transition (Y) elements, respectively. The orange spheres in $C1_b$ stand for the additional stuffing (X) element. (c) The $\Gamma_6 - \Gamma_8$ difference calculated for various Heuslers at their experimental lattice constants. Negative (positive) value means a topological (trivial) insulator. HgTe and CdTe binaries are shown for comparison. Open squares mark the systems not reported in the literature. Pairs of materials with well-matching lattices for the QSH QWs can be easily picked up along the same vertical lines. The borderline compound (between trivial and topological) insulators (YPtSb, YPdBi, ScAuPb) are situated closer to the zero horizontal line. Adapted with permission from [61]. Copyright 2010 Nature Publishing Group.

the results display two striking features. First is that at a low magnetic field a sequence of Hall plateaus develops with odd filling factors $\nu = 9$, 7 and 5, before at a higher field the sequence is continued with $\nu = 4$, 3 and 2. The existence of odd number filling at a low field means that a zero mode, a Landau level at zero energy, is present due to the linear dispersion of two degenerate Dirac fermions from the top and the bottom surfaces. The even number fillings at a higher field are attributed to uneven charge densities on the upper and lower surfaces. Second is that longitudinal resistance minima do not approach zero at the highest magnetic fields. The existence of topological surface states at four side surfaces parallel to the field plausibly explains this backscattering resistance, when the top and bottom surface states are in the quantum Hall transport regime. Additionally, ARPES measurement (figure 13(c)) on a strain relaxed, 1 μm thick HgTe sample revealed a Dirac cone from surface states existing at $\bar{\Gamma}$. This is in accordance with the calculated band structure of the Te termination case [57].

4.2.2. Heusler compounds. Heusler compounds, discovered by Fritz Heusler *et al* [59] one century ago, are a class of ternary materials with XYZ (often called half-Heusler) or X_2YZ stoichiometric composition and having semiconducting or metallic phases (see [60] for review). Their structures can be viewed as stuffing the void spaces in a zinc-blende lattice (like HgTe) with a third element. For example, the XYZ half-Heuslers can be understood as stuffing the $(YZ)^{n-}$ zinc-blende sublattice with an X^{n+} ion, see figure 14. From basic structural and bonding considerations, the X_2YZ Heuslers with 18 or 24 valence electrons and XYZ Heuslers with 18 valence electrons are expected to exhibit semiconducting property with an energy gap. The gap can be tuned by the difference in electronegativity of the constituents and the lattice constant in a wide range from about 4 eV to (LiMgN) down to zero (LaPtBi). Because of the similarity to the TI HgTe in both structural and electronic properties, Heusler materials open a platform to design new TIs [61, 62] by tuning the energy gap and setting the desired band inversion by choosing compounds with appropriate hybridization strength (via the lattice constant) and magnitude of SOC (via the atomic charge).

Using *ab initio* calculations two independent groups [61, 62] predicted that tens of Heusler compounds with a zero gap show a similar band inversion to that of HgTe. See figure 14; the negative energy gap between Γ_6 and Γ_8 bands is strong evidence of band inversion. Their real TI state can be realized by applying strain or designing a proper QW structure. The band structure calculations in [61] suggested that LnPtBi may produce TIs with coexisting magnetism (Ln is a rare earth element, Nd, Sm, Gd, Tb and Dy) and particularly LaPtBi could be a topological superconductor. Soon afterwards, another group [63] reported independently that strained LaPtBi is a strong TI with $\mathbb{Z}_2$ invariants (1;000) as well as other LnPtBi (Ln = Lu, Sc, Y and Th) compounds. Subsequently, more sophisticated *ab initio* calculations using optimized exchange-correlation potential [64, 65] and GW approach [66] have confirmed that a large number of Heuslers are TIs with a

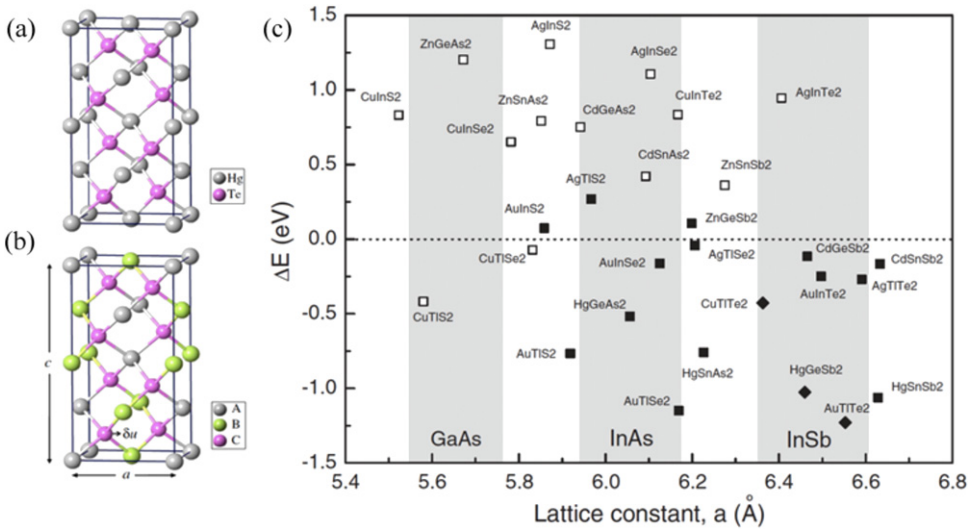

Figure 15. Comparison of the zinc-blende and the chalcopyrite structure. (*a*) The zinc-blende compound HgTe. (*b*) The chalcopyrite compound ABC_2. The tetragonal distortion is characterized by the ratio of lattice constants $\eta = c/2a$, and the internal displacement of the anions C away from the ideal zinc-blende sites is labeled by δu. The AB ordering together with the structural distortion breaks the cubic symmetry. (*c*) Inverted band strength ΔE for various chalcopyrites as a function of the lattice constant. Open symbols mark the compounds whose lattice constants were reported in the literature. For the rest of the compounds their equilibrium lattice constants are obtained by first-principles total energy minimization. When $\Delta E < 0$, squares mark the compounds that are TIs and diamonds mark the systems that are topological metals. Shaded areas indicate materials that are expected to be closely ($\pm 2\%$) lattice matched to either GaAs, InAs or InSb. Adapted with permission from [77]. Copyright 2011 American Physical Society.

band inversion and refined the topological feature of some compounds at the topological phase transition boundary. In addition, a group of Li_2AgSb-class Heuslers are also predicted to be TIs [67].

Recently, an ARPES experiment has measured the surface band structure of three Heuslers, LnPtBi (Ln = Lu, Dy and Gd) [68]. Although metallic surface states were observed in experiments, the topological feature of these states is still not clear due to the ambiguity when compared with their calculated band structure.

As we see, Heuslers discussed above can be viewed as stuffed diamond (zinc-blende) lattice. Analogously, we can stuff the graphite (honeycomb) lattice and get a planar version of Heusler XYZ compounds [69]. These materials have inversion symmetry and hence we can evaluate the parity to look for TI candidates in this new rich family. Density-functional calculations have been carried out on these ternary compounds with a honeycomb lattice [70]. Both parity analysis and surface-state calculations show that many compounds in this family are strong TIs with finely chosen XYZ constituents. Different from HgTe and Heuslers, the band inversion occurs between two p_{xy} bands with opposite parity, instead of between s and p type bands. It is interesting that some compounds with stronger SOC (e.g. KHgSb) are trivial insulators, whereas some with weaker SOC (e.g. LiAuSe) are TIs.

4.2.3. α-Sn, HgSe and β-HgS. The group-IV element Sn in α (also called gray) phase has an inversion-symmetric diamond lattice and the same Γ_6–Γ_8 inverted band structure with a zero gap as HgTe. Following the same logic and confirmed by the parity criteria [20], gray Sn is expected to be a strong TI under uniaxial strain. We notice that HgSe, a close family member of HgTe, also has a similar band inversion [71, 72] with a negative gap -0.20 eV from the experiment [73]. Naturally, we expect that HgSe is a strong TI under strain. But another family member β-phase (zinc-blende) HgS has a different band structure. Local-density-functional (LDA) [74, 75] and LDA-based GW [71] calculations found that HgS has Γ_6 and Γ_8 as valence bands and Γ_7 as the conduction band with a finite energy gap. The spin–orbit splitting gap between Γ_8 and Γ_7 is found to be negative, i.e. Γ_8 ($J = 3/2$) is below Γ_7 ($J = 1/2$). This preserves the Γ_6–Γ_7 band inversion and opens up an energy gap at the same time. Therefore, β-HgS has been predicted recently to be a 3D TI with highly anisotropic surface states [76]. However, the above band-inversion picture is still under debate. Recent GW calculations based on a corrected-LDA method showed that Γ_6 lies in the conduction band without inversion [72].

4.2.4. Chalcopyrite semiconductors. The HgTe-type topological materials discussed above are semimetals and external strain or the QW structure is required to open the gap. Feng *et al* [77] showed a way to naturally break the cubic symmetry in ternary chalcopyrite materials. The ternary ABC_2 chalcopyrite compounds of composition I–III–IV_2 or II–IV–V_2 are isoelectronic analogs of II–V or III–V binary semiconductors, respectively. The crystal structure (space group $D_{2d}^{12} - I\bar{4}2d$) is described as a doubled zinc-blende structure with small structural distortions. As shown in figure 15, A and B atoms are located at different cation sites in each zinc-blende lattice. Due to the structural similarity to their binary analogs, chalcopyrites are expected to closely resemble their electronic states. Some chalcopyrites may become TIs like HgTe. Moreover, the cubic symmetry here is explicitly broken by AB cation ordering and accompanied structural

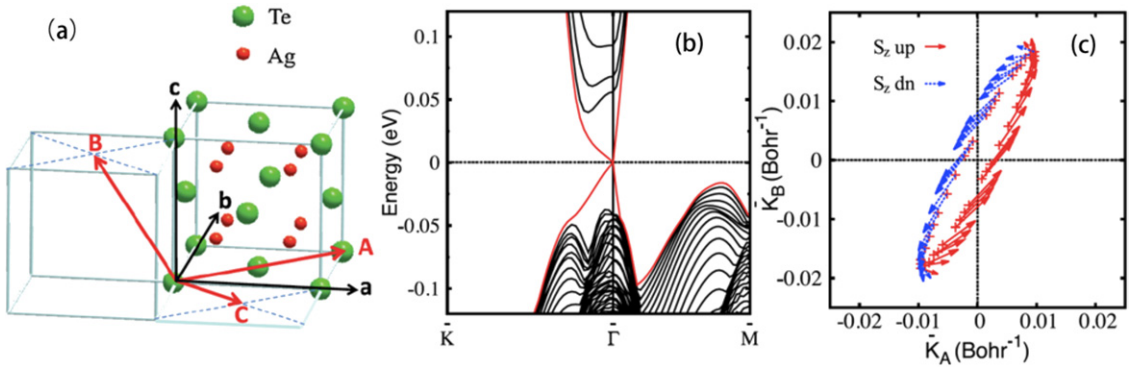

Figure 16. (*a*) Cubic antifluorite structure of α-Ag_2Te and its structural relationship to the β-phase. The lattice vectors of α- and β-phases are labeled a, b, c and A, B, C, respectively. The distortion in β-phase happens in such a way that both the length of A, B, C vectors and the angle between A and B are varied, while keeping C axis perpendicular to the AB plane. The atomic positions are also shifted to the corresponding high-symmetry sites, resulting in a monoclinic structure with space group $P2_1/c$. (*b*) Surface states of β-Ag_2Te for the surface perpendicular to the C axis. The surface band structure and Dirac cone are calculated from a slab of 45 layers; (*c*) FS and spin texture of surface states with chemical potential located 10 meV below the Dirac point. The in-plane components of spin are indicated as arrows, while the red (blue) color means the out-of-plane components pointing out- (in-)ward of the plane. The penetration depth of the surface states is about 3 nm. Adapted with permission from [81]. Copyright 2011 American Physical Society.

distortions. Thereby these new compounds can realize new TIs with a finite energy gap. Feng and co-workers calculated band structures and $\mathbb{Z}_2$ invariants and indeed found a large number of TIs, where the calculated $\mathbb{Z}_2$ invariant [78] agrees well with the intuitive band-inversion picture. Figure 15 shows the band-inversion strength equivalent to the Γ_6–Γ_8 energy difference of HgTe or Heuslers. Negative band-inversion strength indicates they are either TIs or topological metals. Among them, $AuTlS_2$ is found to have a global energy gap 0.14 eV. However, other TI candidates have very small energy gaps, $\sim$10 meV or less. By further tuning the chemical compositions in the same lattice, Chen *et al* [79] reported an optimized version with a larger energy gap reaching to 47 meV. These materials are quaternary I_2–II–IV–VI_4 compounds including $Cu_2HgPbSe_4$, $Cu_2CdPbSe_4$, $Ag_2HgPbSe_4$ and $Ag_2CdPbTe_4$. Recently, Wang *et al* [80] also reported calculations showing that some Cu-based quaternary and ternary chalcogenides are new TI candidates in the same doubled zinc-blende lattice.

4.2.5. α- and β-Ag_2Te. Ag_2Te, known as Hessite mineral in nature, crystallizes in the cubic α-phase at high temperatures and displays a phase transition into the β-phase with structural distortion below 417 K. α-Ag_2Te is found to be a zero-gap semimetal, similar to HgTe, with inverted band ordering. The distortion of β-Ag_2Te can open an energy gap, turning it into a gapped TI [81]. α-Ag_2Te has the antifluorite structure (figure 16(*a*)). It can be viewed as a half-Heusler XYZ structure with $X = Y =$ Ag and $Z =$ Te. Zhang and co-workers [81] performed *ab initio* band structure calculations and found that it indeed has similar band ordering to HgTe and a zero gap. Accordingly, α-Ag_2Te is predicted to be a HgTe-type TI [81]. When the β-phase forms (figure 16(*a*)), the effect of distortion opens a gap ($\sim$80 meV) around the Fermi level while preserving the band inversion. The topological feature is further confirmed by parity analysis in the presence of inversion symmetry. Direct surface-state calculations exhibit Dirac-type surface states with spin chiral texture (figure 16). Different from previous known materials, such as Bi_2Se_3 and Bi_2Te_3, the Dirac cone is highly anisotropic and the Fermi velocity varies by an order of magnitude when the crystal axis is rotated. The existence of linear Dirac-type surface states may also explain an unusually large and nonsaturating linear magnetoresistance observed in silver chalcogenides before [82].

4.2.6. Skutterudites and filled skutterudites (FSs). Skutterudite [84] is the name of a $CoAs_3$-based mineral that was first extensively mined in the region of Skutterud, Norway. Compounds with the same cubic crystal structure have since become known as 'skutterudites'. Figure 17 shows the crystal structure in a bcc lattice. It has two voids in the cubic unit cell. Similar to packing the zinc-blende lattice in Heusler compounds, filled skutterudites (FSs) can be obtained by filling the voids with a variety of atoms including lanthanides (La, Ce, Pr, Nd, Sm, Eu, Gd, Tb). Skutterudites and the filled version FSs have received much interest for their thermoelectric properties, heavy fermion physics and even superconductivity. Recent theoretical studies reveal that some skutterudites are possible HgTe-type candidates for being TIs or near the topological transition boundary. For instance, Pickett and colleagues [85] found $CoSb_3$ is near the transition boundary between trivial insulator and TI. At the critical transition point band inversion occurs between a p-orbital band and a d-orbital band with different parities. To increase the SOC strength, Co is substituted with heavier elements. In particular, $RhSb_3$ and $IrSb_3$ are found to be zero-gap TIs [86]. For FSs, recent calculations [83] predicted that two Ce-based FSs $CeOs_4As_{12}$ and $CeOs_4Sb_{12}$ are TIs with $\mathbb{Z}_2$ invariants (1;000). As shown in figure 17, they have a zero energy gap due to band degeneracy at the Fermi energy and band inversion between a d-orbital band (even parity) and a f-orbital band (odd parity). Thus, $CeOs_4As_{12}$ and $CeOs_4Sb_{12}$ have the potential to be new TIs with coexisting rich physics in FS materials, e.g. Kondo effect, magnetism and superconductivity.

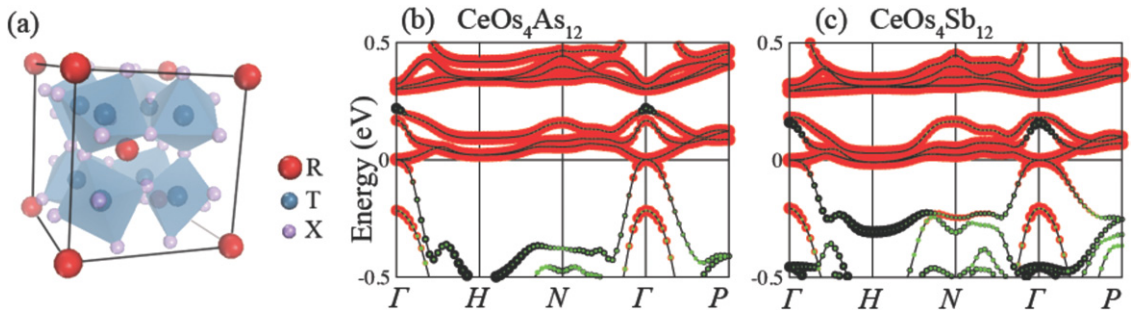

Figure 17. (*a*) Crystal structures in bcc lattice for skutterudites TX_3 (T = Co, Rh, Ir, and X = Sb) and FSs RT_4X_{12} (R = rare-earth, T = Fe, Ru or Os and X = P, As or Sb). Calculated band structures of (*b*) $CeOs_4As_{12}$ and (*c*) $CeOs_4Sb_{12}$. Red dots stand for the components of Ce f-states, black dots for Os d-states and green for p-states. The size of dots represents the relative amplitude of the corresponding components. The Fermi energy is set to zero. A band inversion occurs between the f-orbital band (odd parity) and the d-orbital band (even parity). Adapted with permission from [83]. Copyright 2012 American Physical Society.

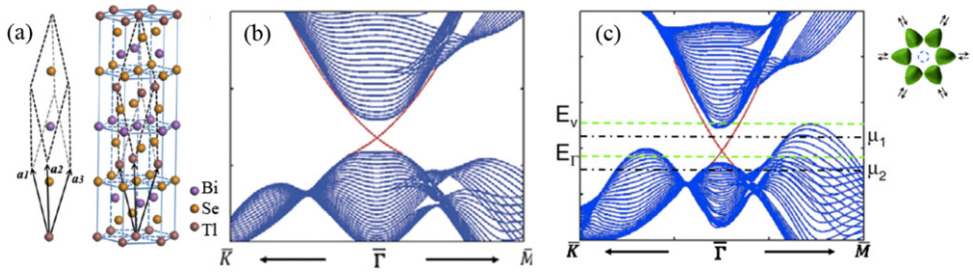

Figure 18. (*a*) Crystal structure of $TlBiSe_2$ with three primitive lattice vectors denoted as a1; 2; 3, including four atoms. The equivalent hexagonal lattice of $TlBiSe_2$ is shown on the right with atomic layers stacked in the sequence –Tl–Se–Bi–Se–. (*b*) The calculated surface states (red line) showing a single Dirac cone for $TlBiSe_2$. The black line shows the band edge for the conduction band and the valence band. The dispersion of surface states is calculated from the effective Hamiltonian equation (10). (*c*) Bulk and surface states of $TlBiTe_2$. E_v and E_Γ are the valence band top in the whole Brillouin zone and at the Γ point, respectively. μ_1 and μ_2 label two typical positions of the chemical potential. On the right we show the FS plot at chemical potential μ_1 and the schematic picture of the He^3-B-type triplet pairing with spin direction correlated with momentum. The inner circle is the FS from the topological surface states and the six leaflike hole pockets are from the p-doped BBs. Adapted with permission from [87]. Copyright 2010 European Physical Society.

4.3. Variation of the Bi_2Se_3 family

The discovery of the Bi_2Se_3 family TIs [17, 22–24] inspired a search for new topological materials guided by requiring strong spin–orbit interaction. Among normal main-group elements in the periodic table, the lower right corner elements Bi, Pb and Tl are cations that have the strongest atomic SOC, and I, Br, Te, Se are anions that have the strongest SOC [26]. Naturally Pb- and Tl-based chalcogenides, which are similar to the Bi_2Se_3 family, attracted the earliest attention. Many of them have since been predicted theoretically to be TIs and some are already verified by experiments. On the other hand, new variations are synthesized by mixing element compositions from the Bi_2Se_3 family, generating excellent TI materials with much better bulk insulating properties than their parent materials.

4.3.1. $TlBiSe_2$ family. Thallium (Tl)-based chalcogenides $TlBiQ_2$ and $TlSbQ_2$ (Q = Te, Se, S) were the first predicted [87–89] 3D TIs and soon observed in experiments [90–93] after the discovery of the Bi_2Se_3 family. They have a rhombohedral crystal structure ($D_{3d}^5 - R\bar{3}m$) similar to Bi_2Se_3. Take $TlBiSe_2$ for example. Atoms are placed in layers with the sequence –Tl–Te–Bi–Te– and the primitive unit cell contains four atoms. We know that Bi_2Se_3 has five atomic layers forming a QL and the coupling between two QLs is very weak, of the van der Waals type [17]. But there is strong coupling between every two atomic layers for $TlBiSe_2$ and the crystal structure is essentially 3D, as shown in figure 18. There is inversion symmetry in the material where Tl and Bi sites act as the inversion center under inversion operation. Yan *et al* discovered the topological feature of these Tl-based materials based on *ab initio* calculations and evaluated the energy dispersion of their topological surface states [87]. $TlBiSe_2$, $TlBiTe_2$ and $TlSbSe_2$ are found to be strong TIs with a large energy gap at the Γ point (∼0.2 eV), however $TlBiTe_2$ is an indirect gap semimetal. $TlBiS_2$, $TlSbTe_2$ and $TlSbS_2$ are small gap insulators near the topological transition boundary. Take $TlBiSe_2$ as an example of a TI. The BB structure exhibits band inversion only at the Γ point between the Bi-p-orbital conduction band (even parity) and the Se-p-orbital valence band (odd parity) when SOC is turned on, resulting in a strong TI with $\mathbb{Z}_2$ invariants (1;000). In contrast, no band inversion occurs for $TlSbS_2$, indicating that $TlSbS_2$ is a trivial insulator with $\mathbb{Z}_2$ invariant (0;000a). Although $TlBiSe_2$-type materials are not layered structures, they share the same crystal symmetry as Bi_2Se_3. Their low-energy states near the Fermi energy are also similar to Bi_2Se_3 and band inversion occurs only at the Γ point. Therefore, the effective Hamiltonian describing the band electrons close to the Fermi energy takes the same form as the model proposed earlier for the Bi_2Se_3 type of materials [17, 18]. To describe the BBs more accurately, we added a k-cubic term to the Hamiltonian

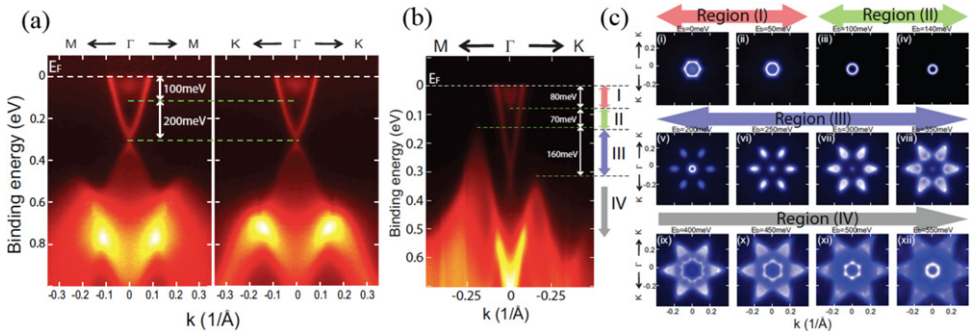

Figure 19. (*a*) ARPES measured band structure of $TlBiSe_2$ along the M–Γ–M and K–Γ–K directions. The isolated Dirac point lies 200 meV below the bulk conduction band (BCB). (*b*) Band dispersions of $TlBiTe_2$ along the M–Γ–K direction. Four regions defined by characteristic energy positions of the band structure are labeled. (*c*) Constant energy plot of the band structure in different regions defined in (*b*), showing the BCB FS inside the SSB (region I), surface state only (region II), BVB outside SSB (region III) and all BVB (region IV). Adapted with permission from [92]. Copyright 2010 American Physical Society.

equation (4). The surface effective Hamiltonian can be derived up to k^3 as

$$H_{\text{surf}} = \tilde{C} + \tilde{D}_2 + \tilde{A}_2(k_x\sigma^y - k_y\sigma^x) + \frac{\tilde{R}_1}{2}(k_+^3 + k_-^3). \quad (10)$$

Here $k_\pm = k_x \pm ik_y$, the parameters $\tilde{C}$, $\tilde{D}_2$, $\tilde{A}_2$ and $\tilde{R}_1$ depend on the details of the boundary condition and material parameters [18, 94]. The calculated topological surface states using the effective $\boldsymbol{k}\cdot\boldsymbol{p}$ Hamiltonian equation (10) are shown for $TlBiSe_2$ and $TlBiTe_2$ in figure 18. A single Dirac cone is found at the $\bar{\Gamma}$ point of the surface Brillouin zone, similar to Bi_2Se_3. One of the most striking properties in this class of TIs is the superconductivity observed in p-doped $TlBiTe_2$ [95]. p-doped $TlBiTe_2$ could inherit the topological properties from the parent TI [87]. On the other hand, those small gap materials $TlBiS_2$, $TlSbTe_2$ and $TlSbS_2$ are on the border of a topological transition where the BBs will form a 3D Dirac cone near the surface. Yan *et al* proposed that a topological phase transition can be driven, e.g. by pressure [87]. Soon afterwards, two independent groups [88, 89] also reported their work on the above Tl-based compounds by *ab initio* calculations and their results agree very well with our work. The surface-state calculations using the slab model show the topological surface states, in which the dispersion behaves sensitively to different surface terminations. The surface state is found to decay into the bulk much slower [89] than in Bi_2Se_3.

Soon after the theoretical prediction [87], $TlBiSe_2$ [90–92] and $TlBiTe_2$ [92] were confirmed by ARPES experiments to be 3D TIs with nontrivial surface states (figure 19). An ideal Dirac cone at the Γ point was observed in the surface band structure for both materials, without trivial dangling bond states that were observed in the slab calculations [88, 89]. This might be attributed to the fact that the cleaved surface in ARPES measurements has various terminations owing to the absence of a natural cleavage plane [90]. Although values are a little varied in different reports, it is clear that $TlBiSe_2$ has a large energy gap (0.2–0.35 eV) [90, 92], much larger than the energy scale of room temperature. Its Dirac cone in the gap is well isolated from the BBs and the Fermi velocity is found to be comparable to that of the Bi_2Se_3 types of materials [90–92]. Further spin-resolved ARPES measurements [93] have confirmed the spin-momentum locking feature of the helical surface states. Compared with the Bi_2Se_3 family, the much improved mechanical properties of $TlBiSe_2$ from strong covalent bonding between atomic layers make it more favorable for real devices. On the other hand, $TlBiTe_2$ is found to be a semimetal with a negative bulk gap, instead of a narrow-gap semiconductor as conventionally believed [96, 97]. Nonetheless, a single Dirac cone still exists in the energy gap of Γ, consistent with our calculation [87]. The observed semimetalicity also solves the mysterious puzzle of the smaller thermoelectric power of $TlBiTe_2$ [98, 99] compared with other compounds in the family, since the coexisting conduction electron and hole pockets cancel each other's thermoelectric contributions. It should be pointed out that the FS is characterized by a single ringlike surface state and six surrounding p-type bulk pockets in region III of figure 19, which is highly consistent with the theoretical calculation [87]. The bulk superconductivity of p-type $TlBiTe_2$ is expected to originate from the six leaflike bulk pockets. In the superconducting state, the surface state (the center FS pocket) can become superconducting due to the proximity effect induced by the bulk superconductivity. Such a superconductor can realize the Majorana fermion in the vortex core [100]. However, the presence of superconductivity in p-type $TlBiTe_2$ requires further confirmation [101]. In addition, recently a topological phase transition was observed [102] in $TlBi(S_{1-\sigma}Se_\sigma)_2$ (also written as $BiTl(S_{1-\sigma}Se_\sigma)_2$) which can be viewed as a mixture of strong TI $TlBiSe_2$ and $TlBiS_2$, which lies on the TI boundary. By increasing the Se composition σ, a transition from a trivial insulator with an energy gap to a TI with gapless surface states is found in ARPES experiments. This topological phase transition further confirms the theoretical prediction of topological phase transitions about these boundary materials [87].

4.3.2. $LaBiTe_3$ family. By simply substituting one cation atom with a rare earth element in the Bi_2Se_3 types of materials, a new class of stoichiometric compound $LnBT_3$ (Ln = rare earth elements, B = Bi, Sb, and T = Te, Se) can be obtained [103]. They share the same layered crystal structure as Bi_2Se_3. We performed *ab initio* calculations [104] for

$LnBiTe_3$ and $LnSbTe_3$ (Ln = rare earth elements La and Y that do not have f electrons), which have already been synthesized in experiments [103], and found that $LaBiTe_3$ is a TI with an energy gap above room temperature (0.07–0.12 eV), whereas the other three materials are trivial insulators or semimetals. This can be understood by the fact that $LaBiTe_3$ has the strongest atomic SOC among these four compounds. Surface-state calculations show Dirac-like topological surface states at $\bar{\Gamma}$. Different from Bi_2Te_3, $LaBiTe_3$ of the simplest crystal structure does not have inversion symmetry and a dipole electric field can exist on the surface. Inversion symmetry breaking and surface dipole field can be tools to engineer the 2D electron gas as well as the surface states. Furthermore, we expect that the band inversion persists in $LnBiTe_3$ when La is substituted with other heavier rare earth elements (Ln = Ce, Pr, ..., Gd, ..., Lu) with f electrons [103], which provides an avenue for bulk magnetic doping in this family to realize a quantum anomalous Hall insulator [105, 106], axionic insulator [43] and topological Kondo insulator [107]. Moreover, the trivial insulators $YBiTe_3$ and $YSbTe_3$ can be employed as protecting barrier materials for both $LaBiTe_3$ and Bi_2Te_3 families for their well-matched lattice constants and chemical composition.

4.3.3. $PbBi_2Se_4$ family. The QL of Bi_2Se_3 has a stacking sequence Se–Bi–Se–Bi–Se. By inserting a double-layer –Pb–Se– into the QL and preserving the inversion symmetry, we can obtain a new compound $PbBi_2Se_4$ with stacking sequence Se–Bi–Se–Pb–Se–Bi–Se. As an extension to this double-layer filling idea, various layered chalcogenides can be derived as $A_nB_{2m}X_{3m+n}$ (A = Pb, Sn and Ge, B = Bi and Sb, X = Te and Se). Most of these compounds have already been synthesized in experiments. For example, $Ge_2Sb_2Te_5$ (called GST) has been extensively studied as a phase-change material and used for data storage in the industry [108]. Recently, both *ab initio* calculations [109–111] and ARPES measurements [109] have revealed that many compounds among $A_nB_{2m}X_{3m+n}$ chalcogenides are TIs, which we call the $PbBi_2Se_4$ family. In calculations, Pb-based compounds $Pb_nBi_2Se_{3+n}$ and $Pb_nSb_2Te_{3+n}$ are found to be TIs for $n = 1, 2$ [109, 110], but trivial insulators for $n \geqslant 3$ [110]. Among them $PbBi_2Se_4$ is reported to have a very large theoretical energy gap, 0.40 eV, and $Pb_2Sb_2Te_5$ is found to be located at the topological phase transition boundary [110]. In addition $PbBi_4Te_7$ [109, 112], $GeBi_2Te_4$ [109, 111, 113], $SnBi_2Te_4$, $SnSb_2Te_4$ and $YbBi_2Te_4$ [113] are also found to be TIs. Not surprisingly, the calculated surface states of these materials have band structures similar to the Bi_2Se_3 family. In experiments, only $GeBi_2Te_4$ has since been confirmed by ARPES [109]. Interestingly, the surface states of $GeBi_2Te_4$ have a well-isolated Dirac point in the bulk gap, different from Bi_2Te_3 in which the Dirac point is buried in the bulk valence bands [23].

4.3.4. Bi_2Te_2Se and $(Bi_{1-x}Sb_x)_2Te_3$. Bi_2Se_3, Bi_2Te_3 and Sb_2Te_3 are the most extensively studied 3D topological materials. However, they are found to have many residual bulk carriers from crystal defects [2, 3] or environmental doping [115–117], hindering transport experiments and the use of their novel topological surface states for practical application. For instance, Bi_2Se_3 is always n-type because of Se vacancies. Bi_2Te_3 is usually rather metallic (n- or p-type) due to Bi–Te anti-site defects, which are promoted by the weakly polarized bond between Bi and Te with a similar electronegativity. Sb_2Te_3 is found to be p-type, due to the Sb–Te anti-sites where Sb substitutes the Te site. This problem remains unsolved despite extensive efforts involving material doping [23, 25, 116, 118–121], nanostructuring [122–124] and electric gating [125, 126]. Based on the understanding of the material properties, it is possible to obtain new ternary or even quaternary compounds by mixing these three materials, aiming to achieve a better bulk insulating property.

Ando and co-workers [55] observed high bulk resistivity (exceeding 1 Ω cm) in Bi_2Te_2Se, which was determined to be a TI by ARPES, with surface states similar to Bi_2Te_3 [109]. Soon Xiong *et al* also reported that they observed even larger resistivity (6 Ω cm) in the same material [127]. The large bulk resistivity can be understood in terms of the suppression of bulk defects. Stoichiometric Bi_2Te_2Se has a stacking sequence of Te–Bi–Se–Bi–Te in a QL. Se is trapped between two BIs and less exposed to evaporation, and hence the formation of Se vacancies is suppressed. The center Se prefers to bind with Bi, instead of Te, and therefore the formation of Te and Bi anti-site defects is also suppressed. Recently, Ando's group [128] synthesized a more complicated alloy $Bi_{1.5}Sb_{0.5}Te_{1.7}Se_{1.3}$ by reduced Te : Se ratio and introducing some Sb into Bi positions, on which they achieved a surface-dominated transport with surface channel contribution up to 70%. The reduced Te : Se ratio is expected to suppress the anti-site defects between Bi and Te. Sb doping [116] is expected to reduce the density of Se vacancies at the outmost layer. Right after surface cleavage, the material shows p-type behavior, i.e. the Fermi energy is below the Dirac point; after a while, air exposure causes *n*-doping to the surface [115], indicated by a sign change in the Hall coefficient with time.

Recently, a nonstoichiometric alloy $(Bi_{1-x}Sb_x)_2Te_3$ has been reported by two independent groups [114, 129]. Sb doping was employed to reduce the bulk carrier density in Bi_2Se_3 [116]. Here increasing Sb composition also acts to shift the Fermi energy down from n-type to p-type carrier regimes [116]. Parallel ARPES measurements indeed show a remarkable tuning of the Fermi energy downward gradually across the Dirac point [114, 129], as shown in figure 20. On the nanotemplate of $(Bi_{1-x}Sb_x)_2Te_3$, Kong *et al* [114] observed a clear ambipolar gating effect similar to that observed in graphene.

4.3.5. $Cu_xBi_2Se_3$, $Pd_xBi_2Te_3$ and strained Bi_2Te_3. In Bi_2Se_3, Cu intercalation in the van der Waals gaps between QLs is found to induce superconductivity at $T_c = 3.8$ K in $Cu_xBi_2Se_3$ for $0.12 \leqslant x \leqslant 0.15$ [130]. Further measurement [131] showed that the topological surface states remain well preserved at the Fermi level of the superconductor where Cooper pairing takes place. On the other hand, Pd-doping in another TI Bi_2Te_3 can also realize superconductivity at T_c up to 5.5 K [132]. Regardless of doping, Bi_2Te_3 is recently reported

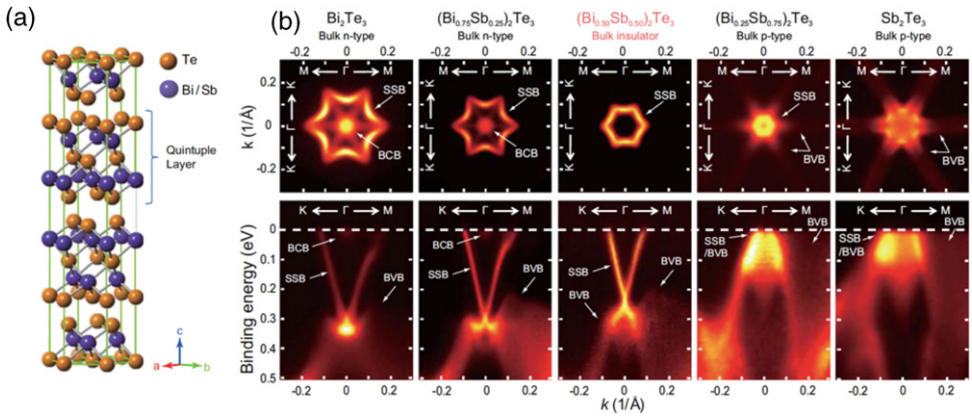

Figure 20. $(Bi_{1-x}Sb_x)_2Te_3$ is a tunable TI system with a single Dirac cone of surface states. (*a*) Tetradymite-type crystal structure of $(Bi_{1-x}Sb_x)_2Te_3$ consists of QLs (∼1 nm in thickness) bonded by van der Waals interactions. (*b*) ARPES FS map (top row) and band dispersion along the K–Γ–M (bottom row) directions from bulk single crystals with nominal compositions of $x = 0.0$, 0.25, 0.50, 0.75 and 1.0. By increasing Sb concentration, the Fermi energy (E_F) exhibits systematic downshift from the bulk conduction band (BCB) to the BVB through a bulk insulating state achieved in $(Bi_{0.5}Sb_{0.5})_2Te_3$. The SSB consists of a single Dirac cone around the Γ point, forming a hexagram FS (top row) and V-shape dispersion in the band structure (bottom row). The apex of the V-shaped dispersion is the Dirac point. Note the shape of the Dirac cone (especially the geometry below the Dirac point, which hybridizes with the BVB) also varies with the Bi/Sb composition. For Bi : Sb ratio less than 50 : 50, as-grown materials become p-type; the E_F resides below the Dirac point thus only the lower part of the Dirac cone is revealed in the ARPES measurement (while the V-shaped dispersion inside the bulk gap is not seen). The n-type SSB pocket on FS shrinks with increasing Sb concentration and eventually becomes a p-type pocket hybridized with the bulk band (BVB) in the Bi : Sb concentrations of 25 : 75 and 0 : 100. Adapted with permission from [114]. Copyright 2011 Nature Publishing Group.

to become superconducting with $T_c \sim 3$ K under pressure 3–6 GPa [133]. The existence of topological surface states in this pressure region is confirmed by *ab initio* calculations based on the strained structure, which is found to be similar to that without pressure. This indicates that it is also possible to realize topological superconductivity in strained Bi_2Te_3.

4.4. Others

4.4.1. AlSb/InAs/GaSb QWs. The 'broken gap' type-II AlSb/InAs/GaSb QWs display an 'inverted' phase similar to HgTe/CdTe QWs and are predicted to exhibit the quantum spin Hall effect [134], i.e. a 2D TI. Figure 21 shows the QW structures. The alignment of the conduction band and valence band edges of InAs and GaSb is unusual here. The valence edge of GaSb is 0.15 eV higher than the conduction edge of InAs. Both are confined between the AlSb barriers. We denote the lowest electron subband as E_1, which is derived from the s-like conduction bands and localized in the InAs layer, and the highest hole subband as H_1, which is derived from p-like heavy-hole bands and localized in the GaSb layer. We focus on a region where E_1 and H_1 bands are nearly degenerate and all other subbands are well separated. When the QW thickness is increased, the E_1 (H_1) band shifts down (up). Above a critical thickness, the E_1 band sinks below H_1, resulting in an inverted band structure with an anti-crossing energy gap [135–137]. Therefore, like HgTe/CdTe QWs, the AlSb/InAs/GaSb QW is a QSH insulator in the inverted regime. Using a $\boldsymbol{k} \cdot \boldsymbol{p}$ Hamiltonian similar to the BHZ model equation (2), Liu *et al* [134] demonstrated the existence of the topological edge states and systematically studied the topological phase transition. Different from HgTe QWs, the quantum phase transition can be tuned by the gate voltage as well as the QW thickness. On the other hand, initial experiments in the AlSb/InAs/GaSb system

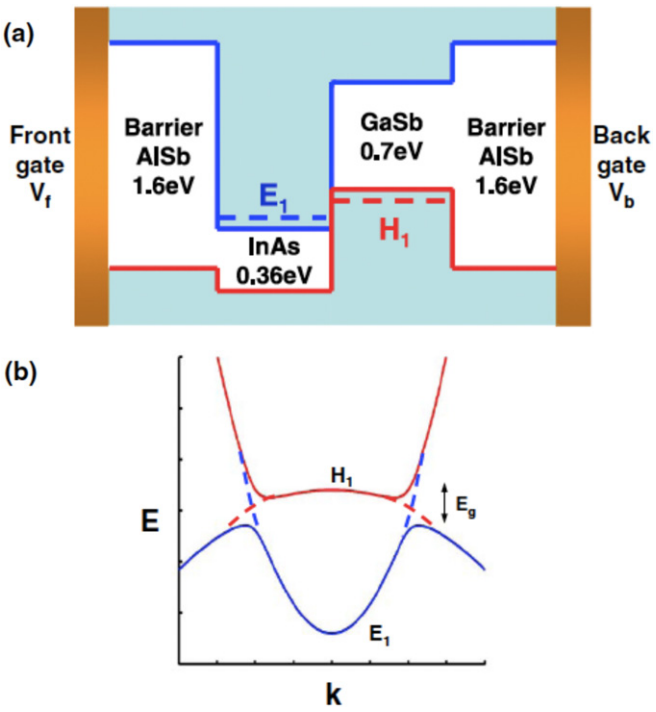

Figure 21. (*a*) Band gap and band offset diagram for asymmetric AlSb/InAs/GaSb QWs. The left AlSb barrier layer is connected to a front gate while the right barrier is connected to a back gate. The E_1 subband is localized in the InAs layer and H_1 is localized in the GaSb layer. Outer AlSb barriers provide an overall confining potential for electron and hole states. (*b*) Schematic band structure diagram. The dashed line shows the crossing of E_1 and H_1 in the 'inverted' regime. Hybridization between E_1 and H_1 opens the gap E_g. Adapted with permission from [134]. Copyright American Physical Society.

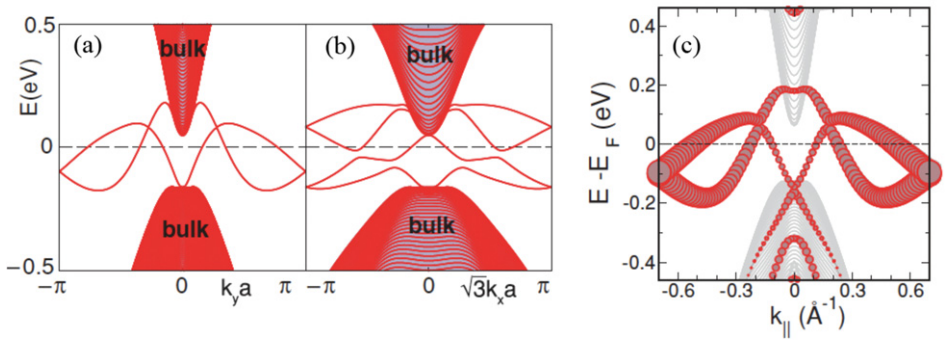

Figure 22. Edge state energy dispersion of the single BL Bi film. Energy bands of the Bi(1 1 1) (*a*) zigzag- and (*b*) armchair-edge ribbons, respectively, with a width of 20 unit cells, calculated from the TB model. (*c*) Energy bands of a eight-unit-cell-wide Bi(1 1 1) zigzag-edge ribbon from first-principles calculations. The size of the symbols corresponds to the weight of the states in the edge atoms. These edge states are found to be more localized at the edge than those of HgTe QWs. Adapted with permission from [148]. Copyright 2011 American Physical Society.

already realize the inverted phase with an energy gap and show encouraging signatures [138, 139].

4.4.2. Graphene, silicene and Bi thin films. In 2005, Kane and Mele investigated the QSH effect in graphene [5], a material with a honeycomb lattice structure. In this insightful work they proposed the $\mathbb{Z}_2$ classification of TR-invariant 2D insulators. Graphene is predicted to be a QSH insulator where SOC coupling opens an energy gap and gapless edge states propagate at the boundary. Unfortunately, the energy gap in graphene caused by intrinsic SOC is insignificantly small [140, 141]. More recently, silicene, a buckled honeycomb lattice of Si, possibly realized on the silver surface in recent experiments [142–144], is reported to be in the QSH phase with a spin–orbit energy gap of 1.55 meV from calculations [145].

A honeycomb lattice of Bi with much stronger SOC was also studied theoretically. Although bulk Bi is a topologically trivial semimetal, both the single-BL Bi film in a buckled honeycomb lattice [146] and multi-BL films [147] are found to be 2D TIs with a larger energy gap by theoretical calculations. Bi crystal has a rhombohedral structure, in which BIs stack in an ABC sequence along the (1 1 1) direction. Each BL forms a hexagonal lattice viewed in the (1 1 1) plane. Using a TB model, Murakami [146] showed that a single-BL Bi has a pair of helical edge states and nontrivial $\mathbb{Z}_2$ number. This prediction was validated by *ab initio* calculations [148]. Topological edge states are found in the bulk gap and intersect the Fermi energy an odd number of times (figure 22). The 2D bulk energy gap is found to be about 0.2 eV. Different from HgTe QWs, the edge state crossing point due to Kramers' degeneracy lies at the 1D Brillouin zone boundary, instead of the center Γ point. In a thin film containing N BLs, N pairs of helical edge states are expected to exist. Thus, multi-BL thin films are expected to be in the QSH phase depending on whether N is odd or even [146]. This speculation is based on the assumption that inter-BL coupling in the film is weak and adiabatically connected to the zero coupling limit [46]. However, Liu *et al* [147] found from *ab initio* calculations that there is strong intermediate inter-BL coupling and surprisingly Bi films of 1–8 BLs thickness are all topologically nontrivial without the odd–even oscillation on thickness. It is interesting to compare the Bi thin film with Bi_2Se_3 or Bi_2Te_3 thin films, which are predicted to be 2D TIs and have trivial–nontrivial oscillation with respect to the film thickness [40, 41]. The oscillation is caused by the band-inversion-induced parity change only at the Γ point. The Bi film has parity changes at all four TRIM due to the strong SOC of Bi when thickness varies, resulting in the preserved nontrivial topological phase.

4.4.3. Strain-engineered materials: PbTe and SnTe, (M_3N)Bi, and Sr_2Pb. PbTe and SnTe are narrow-gap semiconductors with a rocksalt structure. They have a direct energy gap at the four equivalent L points of the fcc Brillouin zone, but an inverted band structure relative to each other. The L_6^- and L_6^+ bands constitute the VBM and CBM of PbTe, respectively, while this ordering is inverted in SnTe. Nonetheless, both of them are trivial insulators according to the parity criteria, since there are four (even number) inversions in the whole Brillouin zone. Fu and Kane [20] proposed a way to make them a strong TI. First, PbTe and SnTe form an alloy $Pb_{1-x}Sb_xTe$. There is an inversion transition at $x \sim 0.4$ where the band gap at the four L points vanishes, in favor of 3D Dirac points. Secondly, applying uniaxial strain along the (1 1 1) direction distinguishes one L point (called T) from the other three L points. At a given x, strain will drive the band-inversion transition at the L and T points. There will be an intermediate phase where L is inverted, but T is not (or vice versa). Because of the odd number of band inversions or parity exchanges, this intermediate phase is a strong TI. It should be noted that this process depends on the uniaxial strain direction. For example, strain along the (1 0 0) direction will distinguish two L points from the other two, and hence will not lead to the topological intermediate phase.

In principle, we can always drive a trivial insulator into a topological phase by tuning material parameters, for example by strain as well as SOC, if it is close to the topological transition point with a small energy gap. Here strain is used to induce the band inversion between the conduction and the valence bands, while it is used only for opening a gap in HgTe (see section 4.2.1). Recently, Chen and his colleagues [149, 150] proposed that several small gap topological trivial materials can be tuned into 3D TIs by uniaxial strain. These

materials are antiperovskite compounds (M_3N)Bi (M = Ca, Sr, Ba) [149] and the Zintl compound Sr_2Pb [150]. Topological surface states and nontrivial $\mathbb{Z}_2$ invariants were observed in their density-functional calculations.

4.4.4. Strongly correlated materials. So far, TI properties were derived from strong SOC, which is a single-particle property. In principle, TIs can also arise from strong correlation effects [151, 152]. There are also other theoretical predictions of new TIs in which the interplay between strong electron–electron interactions and the spin–orbit interaction plays a crucial role. An example is the case of Ir-based materials. Ir is a transition metal with 5d electrons. Ir-based compounds usually exhibit significant SOC effects and electron correlation. The QSH effect has been proposed in Na_2IrO_3 [153]. Na_2IrO_3 has layered structure containing the honeycomb lattice. The TB model analysis together with *ab initio* calculations predicts that it is a layered-QSH system, i.e. a weak 3D TI. Topological Mott insulator phases have been proposed in Ir-based pyrochlore oxides $Ln_2Ir_2O_7$ (Ln = rare earth element) [154–157], and two other pyrochlores $Cd_2Os_2O_7$ [155, 158] and $Cd_2Re_2O_7$ [158]. Furthermore, the topological Kondo insulator phase was proposed with a possible realization in SmB_6 and CeNiSn [107]. Our recently reported TI candidates $CeOs_4As_{12}$ and $CeOs_4Sb_{12}$, containing 4f electrons and found to be Kondo insulators in low-temperature experiments [159, 160], can probably realize the topological Kondo insulator under slight p-type doping [83], in which robust metallic surface states appear in the Kondo gap. Recently, another correlated material α-Fe_2O_3 with corundum structure is predicted to be a possible topological magnetic insulator [161].

5. Conclusion

As we can see from this review, the field of TI materials is growing explosively. The rapid process of material discovery was enabled by precise theoretical predictions, surface sensitive spectroscopies and transport experiments. Future experiments will focus more on novel physical properties of known TI materials, such as dissipationless transport, topological magneto-electric effect and Majorana fermions. These novel effects can only be realized by the interplay between the topological order and conventional order, such as magnetism and superconductivity. The search for strongly correlated TI material will also take center stage in the future, possibly with many surprises to come.

Acknowledgments

The authors would like to thank Martin Claasen for his careful reading of the manuscript and for his useful comments. This work is supported by the ARO under the grant number W911NF-09-1-0508 and by the Keck Foundation.

References

[1] Qi X L and Zhang S C 2010 *Phys. Today* **63** 33
[2] Qi X L and Zhang S C 2011 *Rev. Mod. Phys.* **83** 1057–110
[3] Hasan M Z and Kane C L 2010 *Rev. Mod. Phys.* **82** 3045–67
[4] Moore J 2010 *Nature* **464** 194–8
[5] Kane C L and Mele E J 2005 *Phys. Rev. Lett.* **95** 226801
[6] Bernevig B A and Zhang S C 2006 *Phys. Rev. Lett.* **96** 106802
[7] Bernevig B A, Hughes T L and Zhang S C 2006 *Science* **314** 1757
[8] König M, Wiedmann S, Brüne C, Roth A, Buhmann H, Molenkamp L, Qi X L and Zhang S C 2007 *Science* **318** 766–70
[9] Koenig M, Buhmann H, Molenkamp L W, Hughes T, Liu C X, Qi X L and Zhang S C 2008 *J. Phys. Soc. Japan* **77** 031007
[10] Kane E O 1957 *J. Phys. Chem. Solids* **1** 249
[11] Wu C, Bernevig B A and Zhang S C 2006 *Phys. Rev. Lett.* **96** 106401
[12] Xu C and Moore J E 2006 *Phys. Rev.* B **73** 045322
[13] Murakami S, Iso S, Avishai Y, Onoda M and Nagaosa N 2007 *Phys. Rev.* B **76** 205304
[14] Dai X, Hughes T L, Qi X L, Fang Z and Zhang S C 2008 *Phys. Rev.* B **77** 125319–6
[15] König M 2007 *PhD Thesis* University of Würzburg, Germany
[16] Roth A, Brüne C, Buhmann H, Molenkamp L, Maciejko J, Qi X and Zhang S 2009 *Science* **325** 294
[17] Zhang H, Liu C X, Qi X L, Dai X, Fang Z and Zhang S C 2009 *Nature Phys.* **5** 438–42
[18] Liu C X, Qi X L, Zhang H, Dai X, Fang Z and Zhang S C 2010 *Phys. Rev.* B **82** 045122
[19] Qi X L, Hughes T L and Zhang S C 2008 *Phys. Rev.* B **78** 195424–43
[20] Fu L and Kane C L 2007 *Phys. Rev.* B **76** 045302
[21] Essin A M, Moore J E and Vanderbilt D 2009 *Phys. Rev. Lett.* **102** 146805
[22] Xia Y *et al* 2009 *Nature Phys.* **5** 398–402
[23] Chen Y L *et al* 2009 *Science* **325** 178–81
[24] Hsieh D *et al* 2009 *Phys. Rev. Lett.* **103** 146401
[25] Hsieh D *et al* 2009 *Nature* **460** 1101–5
[26] Wittel K and Manne R 1974 *Theor. Chim. Acta* **33** 347–9
[27] Winkler R 2003 *Spin–Orbit Coupling Effects in Two-Dimensional Electron and Hole Systems* (*Springer Tracts in Modern Physics* vol 191) (Berlin: Springer)
[28] Zhang W, Yu R, Zhang H J, Dai X and Fang Z 2010 *New J. Phys.* **12** 065013
[29] Fu L 2009 *Phys. Rev. Lett.* **103** 266801
[30] Zhang T *et al* 2009 *Phys. Rev. Lett.* **103** 266803
[31] Alpichshev Z, Analytis J G, Chu J H, Fisher I R, Chen Y L, Shen Z X, Fang A and Kapitulnik A 2010 *Phys. Rev. Lett.* **104** 016401
[32] Lee W C, Wu C, Arovas D P and Zhang S C 2009 *Phys. Rev.* B **80** 245439
[33] Zhou X, Fang C, Tsai W F and Hu J 2009 *Phys. Rev.* B **80** 245317
[34] Fang Z and Terakura K 2002 *J. Phys.: Condens. Matter* **14** 3001–14
[35] Perdew J P, Burke K and Ernzerhof M 1996 *Phys. Rev. Lett.* **77** 3865
[36] Marzari N and Vanderbilt D 1997 *Phys. Rev.* B **56** 12847
[37] Souza I, Marzari N and Vanderbilt D 2001 *Phys. Rev.* B **65** 035109
[38] Sancho M P L, Sancho J M L and Rubio J 1984 *J. Phys. F: Met. Phys.* **14** 1205–15
[39] Sancho M P L, Sancho J M L, Sancho J M L and Rubio J 1985 *J. Phys. F: Met. Phys.* **15** 851–8
[40] Liu C X, Zhang H, Yan B, Qi X L, Frauenheim T, Dai X, Fang Z and Zhang S C 2010 *Phys. Rev.* B **81** 041307

[41] Lu H Z, Shan W Y, Yao W, Niu Q and Shen S Q 2010 *Phys. Rev.* B **81** 115407
[42] Zhang Y *et al* 2010 *Nature Phys.* **6** 584–8
[43] Li R, Wang J, Qi X L and Zhang S C 2010 *Nature Phys.* **6** 284–8
[44] Sakamoto Y, Hirahara T, Miyazaki H, Kimura S i and Hasegawa S 2010 *Phys. Rev.* B **81** 165432
[45] Hsieh D, Qian D, Wray L, Xia Y, Hor Y S, Cava R J and Hasan M Z 2008 *Nature* **452** 970–4
[46] Fu L, Kane C L and Mele E J 2007 *Phys. Rev. Lett.* **98** 106803
[47] Moore J E and Balents L 2007 *Phys. Rev.* B **75** 121306
[48] Roy R 2009 *Phys. Rev.* B **79** 195321
[49] Teo J C Y, Fu L and Kane C L 2008 *Phys. Rev.* B **78** 045426
[50] Zhang H J, Liu C X, Qi X L, Deng X Y, Dai X, Zhang S C and Fang Z 2009 *Phys. Rev.* B **80** 085307
[51] Lenoir B A, Dauscher A, Devaux X, Martin-Lopez R, Ravich Y I, Scherrer H and Scherrer S 1996 *Proc. 15th Int. Conf. on Thermoelectrics (Pasadena, CA)* (Piscataway, NJ: IEEE) pp 1–3
[52] Nishide A, Taskin A A, Takeichi Y, Okuda T, Kakizaki A, Hirahara T, Nakatsuji K, Komori F, Ando Y and Matsuda I 2010 *Phys. Rev.* B **81** 041309
[53] Hsieh D *et al* 2009 *Science* **323** 919
[54] Hirahara T, Sakamoto Y, Saisyu Y, Miyazaki H, Kimura S, Okuda T, Matsuda I, Murakami S and Hasegawa S 2010 *Phys. Rev.* B **81** 165422
[55] Taskin A A, Segawa K and Ando Y 2010 *Phys. Rev.* B **82** 121302
[56] Guo H *et al* 2011 *Phys. Rev.* B **83** 201104
[57] Yan B, Zhang H J, X-L Q and Zhang S C unpublished
[58] Brüne C, Liu C X, Novik E G, Hankiewicz E M, Buhmann H, Chen Y L, Qi X L, Shen Z X, Zhang S C and Molenkamp L W 2011 *Phys. Rev. Lett.* **106** 126803
[59] Heusler F, Starck W and Haupt E 1903 *Verh. Dtsch. Phys. Ges.* **5** 220–3
[60] Graf T, Felser C and Parkin S 2011 *Prog. Solid State Chem.* **39** 1
[61] Chadov S, Qi X L, Kübler J, Fecher G H, Felser C and Zhang S C 2010 *Nature Mater.* **9** 541
[62] Lin H, Wray L A, Xia Y, Xu S, Jia S, Cava R J, Bansil A and Hasan M Z 2010 *Nature Mater.* **9** 546
[63] Xiao D, Yao Y, Feng W, Wen J, Zhu W, Chen X Q, Stocks G M and Zhang Z 2010 *Phys. Rev. Lett.* **105** 096404
[64] Al-Sawai W, Lin H, Markiewicz R S, Wray L A, Xia Y, Xu S Y, Hasan M Z and Bansil A 2010 *Phys. Rev.* B **82** 125208
[65] Feng W, Xiao D, Zhang Y and Yao Y 2010 *Phys. Rev.* B **82** 235121
[66] Vidal J, Zhang X, Yu L, Luo J W and Zunger A 2011 *Phys. Rev.* B **84** 041109
[67] Lin H, Wray L, Xia Y, Xu S, Jia S, Cava R, Bansil A and Hasan M 2010 arXiv:1004.0999
[68] Liu C, Lee Y, Kondo T, Mun E D, Caudle M, Harmon B N, Bud'ko S L, Canfield P C and Kaminski A 2011 *Phys. Rev.* B **83** 205133
[69] Casper F, Felser C, Seshadri R, Peter Sebastian C and Pöttgen R 2008 *J. Phys. D: Appl. Phys.* **41** 035002
[70] Zhang H J, Chadov S, Müchler L, Yan B, Qi X L, Kübler J, Zhang S C and Felser C 2011 *Phys. Rev. Lett.* **106** 156402
[71] Fleszar A and Hanke W 2005 *Phys. Rev.* B **71** 045207
[72] Moon C Y and Wei S H 2006 *Phys. Rev.* B **74** 045205
[73] Madelung O (ed) 1982 *Semiconductors: Technology of III-V, II–VI and Non-Tetrahedrally Bonded Compounds* (*Landolt–Börnstein Group III* vol 17, part D) (Berlin: Springer)
[74] Delin A 2002 *Phys. Rev.* B **65** 153205
[75] Cardona M, Kremer R K, Lauck R, Siegle G, Muñoz A and Romero A H 2009 *Phys. Rev.* B **80** 195204
[76] Virot F M C, Hayn R, Richter M and van den Brink J 2011 *Phys. Rev. Lett.* **106** 236806
[77] Feng W, Xiao D, Ding J and Yao Y 2011 *Phys. Rev. Lett.* **106** 016402
[78] Fukui T and Hatsugai Y 2007 *J. Phys. Soc. Japan* **76** 053702
[79] Chen S, Gong X, Duan C, Zhu Z, Chu J, Walsh A, Yao Y, Ma J and Wei S 2011 *Phys. Rev.* B **83** 245202
[80] Wang Y, Lin H, Das T, Hasan M and Bansil A 2011 arXiv:1106.3316
[81] Zhang W, Yu R, Feng W, Yao Y, Weng H, Dai X and Fang Z 2011 *Phys. Rev. Lett.* **106** 156808
[82] Xu R *et al* 1997 *Nature* **390** 57–9
[83] Yan B, Müchler L, Qi X, Zhang S and Felser C 2012 *Phys. Rev.* B **85** 165125
[84] Sales B C 2003 *Handbook on the Physics and Chemistry of Rare Earths* vol 33 (Amsterdam: Elsevier) pp 1–34
[85] Smith J C, Banerjee S, Pardo V and Pickett W E 2011 *Phys. Rev. Lett.* **106** 056401
[86] Müchler L, Yan B, Qi X L, Zhang S C and Felser C unpublished
[87] Yan B, Liu C X, Zhang H J, Yam C Y, Qi X L, Frauenheim T and Zhang S C 2010 *Europhys. Lett.* **90** 37002
[88] Lin H, Markiewicz R S, Wray L A, Fu L, Hasan M Z and Bansil A 2010 *Phys. Rev. Lett.* **105** 036404
[89] Eremeev S, Koroteev Y and Chulkov E 2010 *JETP Lett.* **91** 594–8
[90] Sato T, Segawa K, Guo H, Sugawara K, Souma S, Takahashi T and Ando Y 2010 *Phys. Rev. Lett.* **105** 136802
[91] Kuroda K *et al* 2010 *Phys. Rev. Lett.* **105** 146801
[92] Chen Y L *et al* 2010 *Phys. Rev. Lett.* **105** 266401
[93] Xu S *et al* 2010 arXiv:1008.3557
[94] Shan W Y, Lu H Z and Shen S Q 2010 *New J. Phys.* **12** 043048
[95] Hein R A and Swiggard E M 1970 *Phys. Rev. Lett.* **24** 53–5
[96] Chrissafis K, Vinga E, Paraskevopoulos K and Polychroniadis E 2003 *Phys. Stat. Solidi* a **196** 515–22
[97] Hoang K and Mahanti S D 2008 *Phys. Rev.* B **77** 205107
[98] Spitzer D and Sykes J 1966 *J. Appl. Phys.* **37** 1563–6
[99] Kurosaki K, Kosuga A and Yamanaka S 2003 *J. Alloys Compounds* **351** 279–82
[100] Fu L and Kane C L 2008 *Phys. Rev. Lett.* **100** 096407
[101] Jensen J D, Burke J R, Ernst D W and Allgaier R S 1972 *Phys. Rev.* B **6** 319–27
[102] Xu S *et al* 2011 *Science* **332** 560
[103] Madelung O, Rössler U and Schulz M 2000 *Ternary Compounds, Organic Semiconductors* (*Landolt–Börnstein Condensed Matter Group III* vol 41E) (Berlin: Springer) pp 471–7
[104] Yan B, Zhang H J, Liu C X, Qi X L, Frauenheim T and Zhang S C 2010 *Phys. Rev.* B **82** 161108
[105] Liu C X, Qi X L, Dai X, Fang Z and Zhang S C 2008 *Phys. Rev. Lett.* **101** 146802
[106] Yu R, Zhang W, Zhang H, Zhang S, Dai X and Fang Z 2010 *Science* **329** 61–4
[107] Dzero M, Sun K, Galitski V and Coleman P 2010 *Phys. Rev. Lett.* **104** 106408
[108] Wuttig M and Yamada N 2007 *Nature Mater.* **6** 824–32
[109] Xu S Y *et al* 2010 arXiv:1007.5111
[110] Jin H *et al* 2011 *Phys. Rev.* B **83** 041202(R)
[111] Kim J, Kim J and Jhi S H 2010 *Phys. Rev.* B **82** 201312
[112] Eremeev S, Koroteev Y and Chulkov E 2010 *JETP Lett.* **92** 161–5
[113] Menshchikova T, Eremeev S, Koroteev Y, Kuznetsov V and Chulkov E 2011 *JETP Lett.* **93** 15–20
[114] Kong D *et al* 2011 *Nature Nanotech.* **6** 705–9
[115] Analytis J G, Chu J H, Chen Y, Corredor F, McDonald R D, Shen Z X and Fisher I R 2010 *Phys. Rev.* B **81** 205407
[116] Analytis J, McDonald R, Riggs S, Chu J, Boebinger G and Fisher I 2010 *Nature Phys.*

[117] Kong D *et al* 2011 *ACS Nano* **5** 4698–703
[118] Hor Y S, Richardella A, Roushan P, Xia Y, Checkelsky J G, Yazdani A, Hasan M Z, Ong N P and Cava R J 2009 *Phys. Rev.* B **79** 195208
[119] Checkelsky J G, Hor Y S, Liu M H, Qu D X, Cava R J and Ong N P 2009 *Phys. Rev. Lett.* **103** 246601
[120] Qu D, Hor Y, Xiong J, Cava R and Ong N 2010 *Science* **329** 821
[121] Wang Z, Lin T, Wei P, Liu X, Dumas R, Liu K and Shi J 2010 *Appl. Phys. Lett.* **97** 042112
[122] Peng H, Lai K, Kong D, Meister S, Chen Y, Qi X, Zhang S, Shen Z and Cui Y 2009 *Nature Mater.* **9** 225–9
[123] Sacepe B, Oostinga J, Li J, Ubaldini A, Couto N, Giannini E and Morpurgo A 2011 *Nature Comm.* **2** 575
[124] Xiu F *et al* 2011 *Nature Nanotechnol.* **6** 216–21
[125] Chen J *et al* 2010 *Phys. Rev. Lett.* **105** 176602
[126] Kong D, Dang W, Cha J, Li H, Meister S, Peng H, Liu Z and Cui Y 2010 *Nano Lett.* **10** 2245–50
[127] Xiong J, Petersen A, Qu D, Hor Y, Cava R and Ong N 2012 *Physica* E **44** 917–20
[128] Taskin A, Ren Z, Sasaki S, Segawa K and Ando Y 2011 *Phys. Rev. Lett.* **107** 16801
[129] Zhang J *et al* 2011 *Nature Comm.* **2** 574
[130] Hor Y S, Williams A J, Checkelsky J G, Roushan P, Seo J, Xu Q, Zandbergen H W, Yazdani A, Ong N P and Cava R J 2010 *Phys. Rev. Lett.* **104** 057001
[131] Wray L, Xu S, Xia Y, San Hor Y, Qian D, Fedorov A, Lin H, Bansil A, Cava R and Hasan M 2010 *Nature Phys.* **6** 855–9
[132] Hor Y, Checkelsky J, Qu D, Ong N and Cava R 2010 *J. Phys. Chem. Solids*
[133] Zhang J *et al* 2011 *Proc. Natl Acad. Sci.* **108** 24
[134] Liu C, Hughes T L, Qi X L, Wang K and Zhang S C 2008 *Phys. Rev. Lett.* **100** 236601
[135] Altarelli M 1983 *Phys. Rev.* B **28** 842–5
[136] Yang M J, Yang C H, Bennett B R and Shanabrook B V 1997 *Phys. Rev. Lett.* **78** 4613–16
[137] Lakrimi M, Khym S, Nicholas R J, Symons D M, Peeters F M, Mason N J and Walker P J 1997 *Phys. Rev. Lett.* **79** 3034–7
[138] Knez I, Du R R and Sullivan G 2010 *Phys. Rev.* B **81** 201301
[139] Knez I, Du R R and Sullivan G 2011 *Phys. Rev. Lett.* **107** 136603
[140] Min H, Hill J E, Sinitsyn N A, Sahu B R, Kleinman L and MacDonald A H 2006 *Phys. Rev.* B **74** 165310
[141] Yao Y, Ye F, Qi X L, Zhang S C and Fang Z 2007 *Phys. Rev.* B **75** 041401
[142] Aufray B, Kara A, Vizzini S, Oughaddou H, Léandri C, Ealet B and Le Lay G 2010 *Appl. Phys. Lett.* **96** 183102
[143] De Padova P *et al* 2010 *Appl. Phys. Lett.* **96** 261905
[144] Lalmi B, Oughaddou H, Enriquez H, Kara A, Vizzini S, Ealet B and Aufray B 2010 *Appl. Phys. Lett.* **97** 223109
[145] Liu C C, Feng W and Yao Y 2011 *Phys. Rev. Lett.* **107** 076802
[146] Murakami S 2006 *Phys. Rev. Lett.* **97** 236805
[147] Liu Z, Liu C, Wu Y, Duan W, Liu F and Wu J 2011 *Phys. Rev. Lett.* **107** 136805
[148] Wada M, Murakami S, Freimuth F and Bihlmayer G 2011 *Phys. Rev.* B **83** 121310
[149] Sun Y, Chen X Q, Yunoki S, Li D and Li Y 2010 *Phys. Rev. Lett.* **105** 216406
[150] Sun Y, Chen X, Li D, Franchini C, Yunoki S, Li Y and Fang Z 2011 arXiv:1105.5841
[151] Raghu S, Qi X L, Honerkamp C and Zhang S C 2008 *Phys. Rev. Lett.* **100** 156401
[152] Zhang Y, Ran Y and Vishwanath A 2009 *Phys. Rev.* B **79** 245331
[153] Shitade A, Katsura H, Kuneš J, Qi X L, Zhang S C and Nagaosa N 2009 *Phys. Rev. Lett.* **102** 256403
[154] Pesin D and Balents L 2010 *Nature Phys.* **6** 376–81
[155] Guo H M and Franz M 2009 *Phys. Rev. Lett.* **103** 206805
[156] Yang B J and Kim Y B 2010 *Phys. Rev.* B **82** 085111
[157] Wan X, Turner A M, Vishwanath A and Savrasov S Y 2011 *Phys. Rev.* B **83** 205101
[158] Kargarian M, Wen J and Fiete G A 2011 *Phys. Rev.* B **83** 165112
[159] Bauer E, Slebarski A, Freeman E, Sirvent C and Maple M 2001 *J. Phys.: Condens. Matter* **13** 4495
[160] Baumbach R, Ho P, Sayles T, Maple M, Wawryk R, Cichorek T, Pietraszko A and Henkie Z 2008 *Proc. Natl Acad. Sci.* **105** 17307
[161] Wang J, Li R, Zhang S C and Qi X L 2011 *Phys. Rev. Lett.* **106** 126403